[American Journal of Science, Vol. 317, October, 2017, P. 861–900, DOI 10.2475/08.2017.01]

American Journal of Science

OCTOBER 2017

OXYGEN, CLIMATE AND THE CHEMICAL EVOLUTION OF A 1400 MILLION YEAR OLD TROPICAL MARINE SETTING

XIAOMEI WANG[*], SHUICHANG ZHANG[*], HUAJIAN WANG[*], CHRISTIAN J. BJERRUM[**], EMMA U. HAMMARLUND[***], EMMA R. HAXEN[**], JIN SU[*], YU WANG[*], and DONALD E. CANFIELD[***,§,†]

ABSTRACT. The Xiamaling Formation is an exceptionally well-preserved sedimentary succession deposited on a marine passive margin about 1400 million years ago. We used a multi-proxy approach, including iron speciation, trace metal dynamics, and organic geochemistry, to explore the evolution of ocean chemistry through most of the Xiamaling Formation. This evolution is put in the context of the paleogeography and the sedimentological evolution of the Xiamaling depositional system.

Overall, the Xiamaling Formation is informally divided into six units based on both sedimentological and geochemical criteria. Of the six units, we fully explored four of them. Unit 4, the lowest unit we studied, is comprised of deep-water red muds, periodically interrupted by green-colored silt and sandy turbidites. Iron extraction results show that the red muds are enriched in highly reactive iron, indicating a water-column source for the iron. However, the low organic carbon contents, low hydrogen index (HI) values, and the oxidized nature of the reactive iron pool indicate deposition in oxygenated bottom waters. We interpret unit 4 to represent a low-productivity ferruginous oxygen-minimum zone (OMZ) environment, underlain by oxygenated bottom waters. The transition to unit 3 reflects an increase in primary productivity, and the development of a more biologically active OMZ, that supported anoxygenic phototrophic bacteria. Still, in this unit, the bottom waters remained oxygenated. The overlying unit 2 represents the transition to deep-water deoxygenation and anoxic waters at the sediment surface. These waters were ferruginous in the bottom part of the unit and sulfidic (euxinic) towards the top. In the uppermost unit 1, euxinic conditions continued, punctuated by more frequent water-column oxygenation towards the upper part of the unit.

We place the evolution of these chemical dynamics in the context of climate and climate change, and in particular, the placement of the Xiamaling Formation in relation to the Intertropical Convergence Zone (ITCZ) and the resulting Hadley Cell dynamics. Also, while our results demonstrate the persistence of anoxic water-column conditions high in the water column during the deposition of the Xiamaling Formation, they also demonstrate bottom water oxygenation near the seafloor during the deposition of three of the four units, and over a time interval extending to 10's of millions of years.

Key words: oxygen, Mesoproterozoic, marine, atmosphere, euxinic, OMZ, ferruginous, anoxygenic photosynthesis

* Key Laboratory of Petroleum Geochemistry, Research Institute of Petroleum Exploration and Development, China National Petroleum Corporation, Beijing 100083, China

** Department of Geosciences and Natural Resource Management, Section of Geology, and Nordic Center for Earth Evolution (NordCEE), ØsterVoldgade 10, 1350 København K, Denmark

*** Institute of Biology and Nordic Center for Earth Evolution (NordCEE), University of Southern Denmark, Campusvej 55, 5230 Odense M, Denmark

§ Villum Investigator

† Corresponding author: dec@biology.sdu.dk

INTRODUCTION

The Mesoproterozoic Era (1600–1000 million years ago, Ma) was a time of emerging eukaryote ecosystems (Javaux, 2011; Knoll, 2014; Butterfield, 2015; Cohen and Macdonald, 2015) as well as eukaryote multicellularity (Butterfield, 2000). These evolutionary innovations occurred in an environment that is poorly understood. There is broad disagreement on concentrations of atmospheric oxygen during this Era, with some estimates suggesting very low concentrations of < 0.1 percent present atmospheric levels (PAL) (Planavsky and others, 2014), whereas others suggest minimum levels of ≥ 4 percent PAL (Zhang and others, 2016b; Zhang and others, 2017). Furthermore, the available evidence, while limited, shows wide variability in ocean chemistry. For example, geochemical analyses of sediments from the 1400 to 1500 Ma Roper Group, representing an intra-cratonic basin from Northern Australia, show a water-depth related transition from apparently oxygenated shallow waters to sulfidic (euxinic) deep waters (Shen and others, 2003). Deep-water sediments from the 1000 to 1270 Ma Byland Supergroup, Canada, and the *ca.* 1460 Ma Newland Formation of the Belt Supergroup, North-western US, show mixed sulfidic to ferruginous (Fe^{2+}-enriched water column) conditions (Planavsky and others, 2011), while the deep-water ~1420 Ma Kaltasy Formation, central Russia, displays geochemical signals consistent with oxic bottom-water conditions (Sperling and others, 2014). The 1100 Ma Atar and El Mreiti Groups, Mauritania, deposited in an epicontinental sea, and here, the nearshore sediments record oxic depositional conditions, while the offshore environments record a mix of water-column conditions ranging from oxic to euxinic (Gilleaudeau and Kah, 2015). The *ca.* 1100 Ma Vazante Group, Brazil, houses a number of glacial diamictites, and the postglacial shales of the Morro do Calcário Formation deposited in a mix of oxic and anoxic, sometimes euxinic, water-column conditions (Geboy and others, 2013).

Is this variability in ocean chemistry temporal or spatial, and should it be considered normal for the Mesoproterozoic Era? What drives such variability, and more broadly, how might such variability be related to atmospheric oxygen concentrations? It may prove difficult to answer these questions for every Mesoproterozoic sequence, but the *ca.* 1400 Ma Xiamaling Formation of Northern China offers a rare opportunity to explore transitions in ocean chemistry and biogeochemical environment over a time scale well exceeding 10 million years. Furthermore, we can relate these transitions to the specifics of the Xiamaling depositional environment and its relationship to climate and climate change. The current contribution takes a multiproxy approach, complementing other recent studies on the Xiamaling Formation (Zhang and others, 2015; Zhang and others, 2016b; Zhang and others, 2017), by exploring the dynamics of ocean chemistry through nearly the entire depositional history of the Xiamaling Formation, and by further examining relationships between ocean chemistry and atmospheric oxygen concentrations.

Geologic Setting

The Xiamaling Formation is part of a Paleoproterozoic to mid-Mesoproterozoic sedimentary package deposited on Paleoproterozoic crystalline rocks of the North China craton, where the crystalline rocks were likely formed during the assembly of supercontinent Columbia (Nuna) (Meng and others, 2011) (fig. 1A). Sediments of the Changcheng Group began to deposit approximately 1800 million years ago directly onto the crystalline basement rocks. The oldest of these sediments, the Changzhougou Formation, is predominantly bedded quartz arenites, representing deposition in the littoral zone with possible influence from fluvial and alluvial input. The overlying Chuanlinggou Formation consists of predominantly fine-grained mudstones representing offshore deposition and thus a relative deepening of the basin. The Chuanlinggou rocks transition into dolostones of the overlying Tuanshanzi Formation and thus

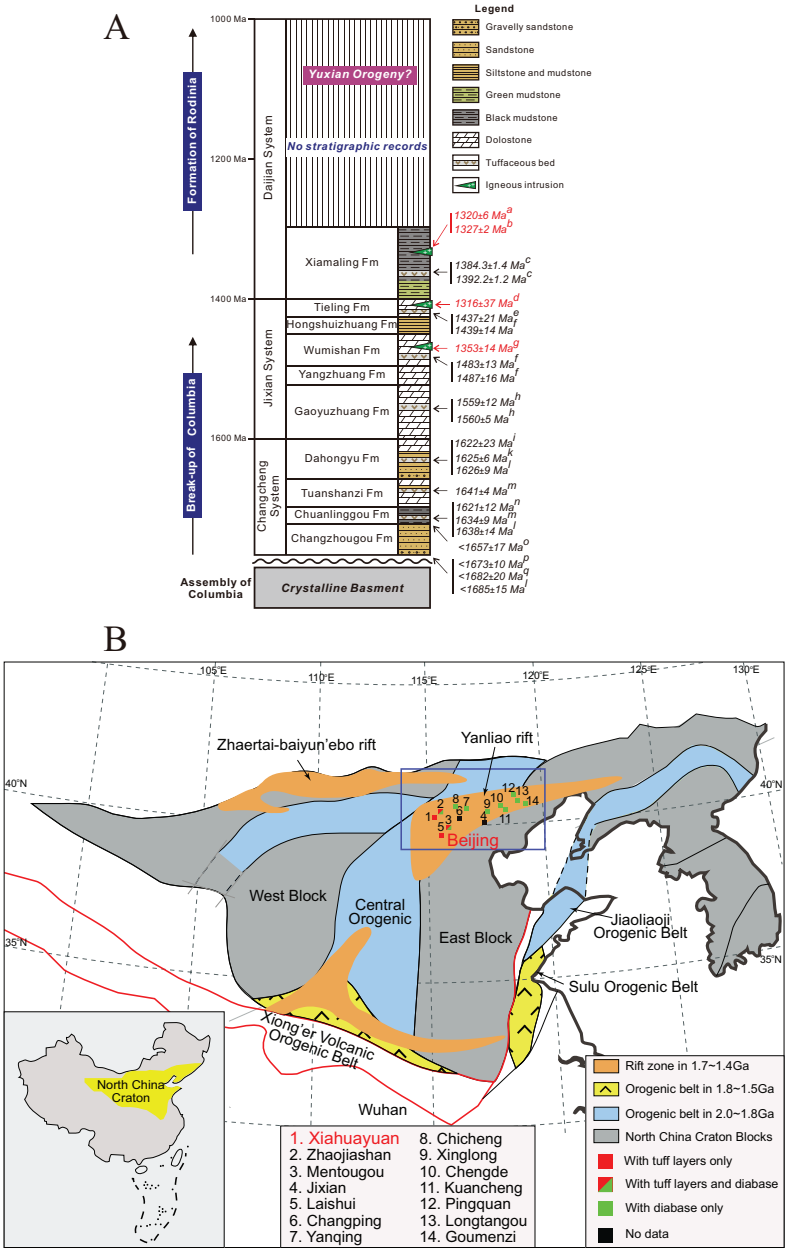

Fig. 1. (A) General geology of the North China Block. Dating from a-(Li and others, 2009), b-(Liu and others, 2011), c-(Zhang and others, 2015), d-(Zhang, Zhao, and Santosh, 2012), e-(Su and others, 2010), f-(Li and others, 2014), g-(Zhang and others, 2009), h-(Li and others, 2010), i-(Lu and others, 2008), k-(Lu and Li, 1991), l-(Gao and others, 2008), m-(Zhang and others, 2013), n-(Sun and others, 2013), o-(Duan and others, 2014), p-(Li and others, 2011), q-(He and others, 2011); dates in red are for intrusive rocks; (B) general map of the North China Block, with a rectangle showing the region of the Xiamaling Formation and numbers designate the different outcrops while the symbols designate their relationship to volcanism.

record a shallowing of the basin into a marine carbonate platform (Meng and others, 2011). All of these sediments contain occasional volcanoclastics, and the whole sequence is interpreted as an opening rift (Meng and others, 2011; Qu and others, 2014).

The top of the Tuanshanzi Formation is marked by an unconformity (Qu and others, 2014). The overlying Nankou Group, beginning with the Dahongyu Formation, deposited in a high-energy, shallow-water environment, with abundant volcanoclastics consistent with continued deposition in a rift environment. In contrast, the overlying Gaoyuzhuang Formation is barren of volcanoclastics and, while still representing shallow-water deposition with abundant stromatolites and dolostones (Zhu and others, 1978), it is believed to represent the transition to a passive margin setting (Meng and others, 2011; Qu and others, 2014).

The Jixian Group overlies the Nankou Group and contains both carbonates and mudstones. The dolostones of the lowermost Yangzhuang Formation are believed to represent inter- and super-tidal deposition, giving way to the dolostones and stromatolites of the overlying Wumishan Formation, and the mudstones of the Hongshuizhuang Formation through relative sea level rise. The Tieling Formation, uppermost in the Jixian Group, represents a stromatolite-bearing carbonate platform developed through an episode of sea-level fall (Meng and others, 2011).

The Xiamaling Formation

The Xiamaling Formation lies both conformably and unconformably over the Tieling Formation (fig. 1A) (Qu and others, 2014). The Xiamaling Formation was once grouped together with the Neoproterozoic Qingbaikou Group, but has subsequently been dated to a Mesoproterozoic age of about 1400 million years (Gao and others, 2008; Su and others, 2008; Li and others, 2013). Recent high-precision zircon ages obtained by isotope dilution Thermal Ionization Mass Spectrometry (TIMS) have further refined the age of the Xiamaling Formation to 1384 ± 1.4 Ma for a tuff layer located in unit 2 (fig. 2) and 1392.2 ± 1.0 Ma for a bentonite layer at the top of unit 3, located 52 m below the tuff layer in stratigraphic height (Zhang and others, 2015). The Xiamaling Formation can be seen in outcrop in several places on the North China Platform (fig. 1B) with a present-day subsurface areal extent estimated at 60,000 km^2 (Fan, 2015). We divide the Xiamaling Formation informally into 6 units. Other schemes propose fewer divisions (Fan, 2015), but ours follows the geochemical and sedimentological observations in the Xiahuayuan area. We present a composite stratigraphy for the Xiamaling Formation in figure 2, generated mainly from outcrop observations, but also from core observations, especially for unit 5. Outcrop and core locations are presented in figure A1 (Appendix). The collection of core material is described below.

The lowermost Xiamaling Formation consists of rock types ranging from conglomerates to sandy shales (Qu and others, 2014), but all rocks indicate deposition in a shallow high-energy environment. In the region of Xiahuayuan, unit 6, where exposed, consists of cross-bedded sands (fig. 3A), giving way to alternating ferruginous and non-ferruginous silts, with occasional ferruginous concretions (fig. 3B), similar to those reported by Zhu and others (2013). Unit 5 consists of brown marlstones, some massive, and interbedded with laminated and organic-poor silts, sands and muds.

Unit 4 is defined, mostly, by alternating red and green muds and green sandy silts (fig. 3C), with occasional sand layers. The green layers vary in thickness from $<$ 1 mm to 4 to 5 cm, but are typically in the 1 to 2 cm range (figs. 3C and 3D). These layers often form erosional contact with underlying muds (fig. 3O) and frequently fine upwards. Unlike the muds, which are unlaminated, the sandy silts are typically parallel laminated, but sometimes show cross stratification (fig. 3E). The red-green banding is

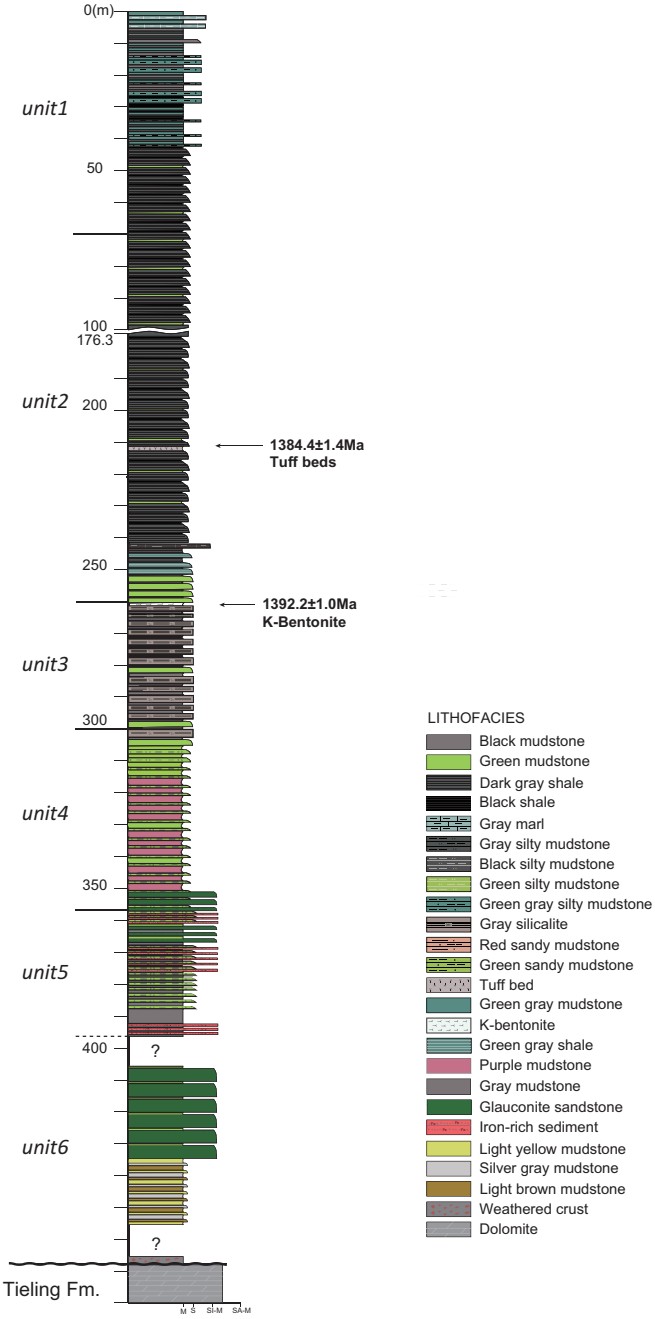

Fig. 2. Measured section of the Xiamaling Formation. Dates from Zhang and others (2015). This is a composite section made from field observation for most of the units except unit 5 where core observations were used. Locations of coring and outcrop sites are found in figure 1A.

not strictly controlled by sedimentology, and the green color from the sandy silts generally "bleeds" both upwards and downwards into the red muds, thereby generating the green muds in this part of the unit (figs. 3D and 3P). We interpret the green

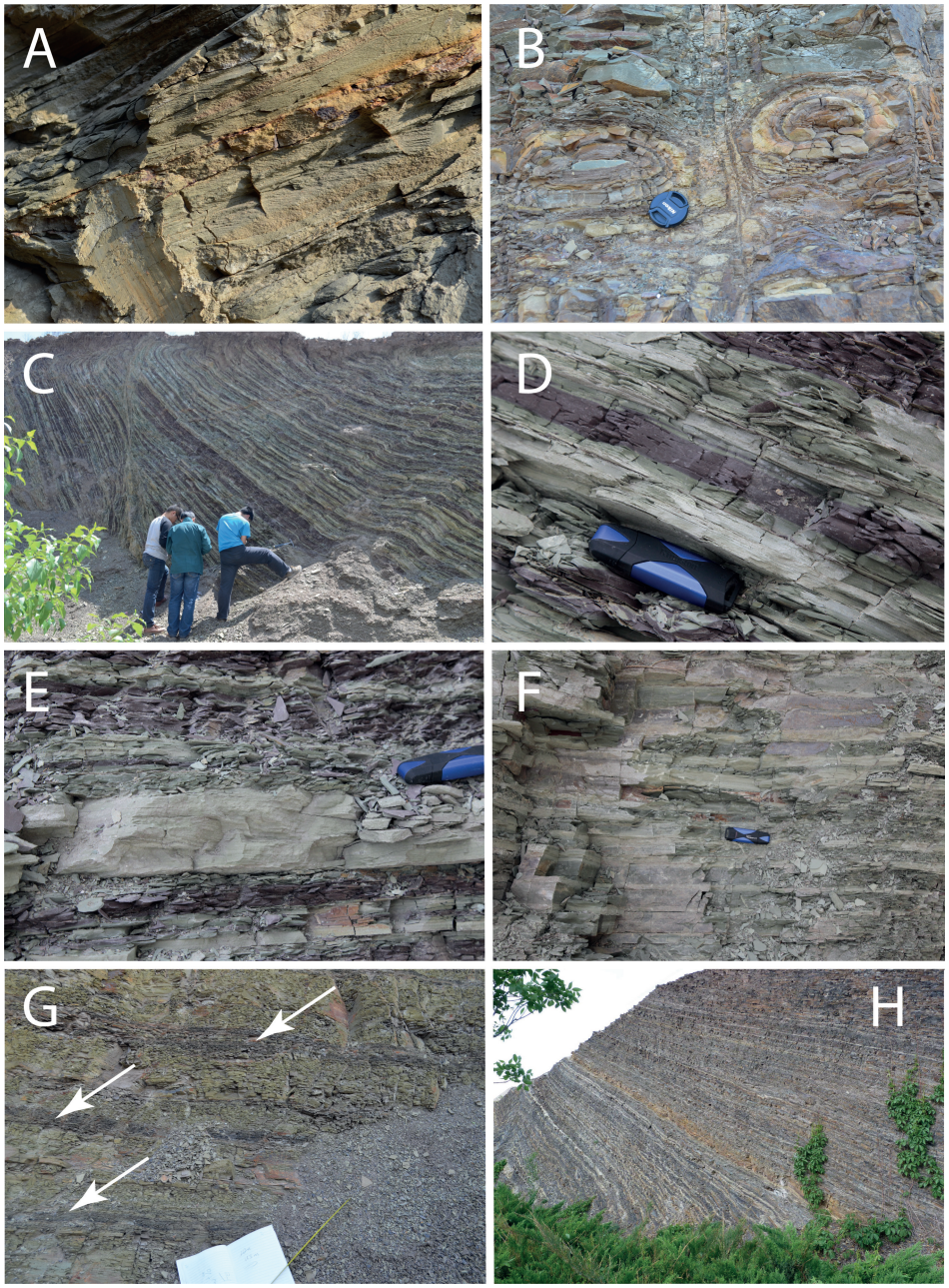

Fig. 3. Outcrop and thin section photos: (A) cross-laminated sandstones from unit 6, (B) concretion layer in the middle of unit 6, (C) alternating red and green layers in unit 4, (D) close-up of green and red layer alternation, showing the "bleeding" of green color from both below and above into the red mud, (E) cross-laminated sandstone towards the top of unit 4. (F) Alternating green muds and sand/silt units above the last red sediment in unit 4, (G) the development of the first black shales (white arrows) within background green mud, indicating the beginning of unit 3 deposition, (H) typical layered sediments from unit 3.

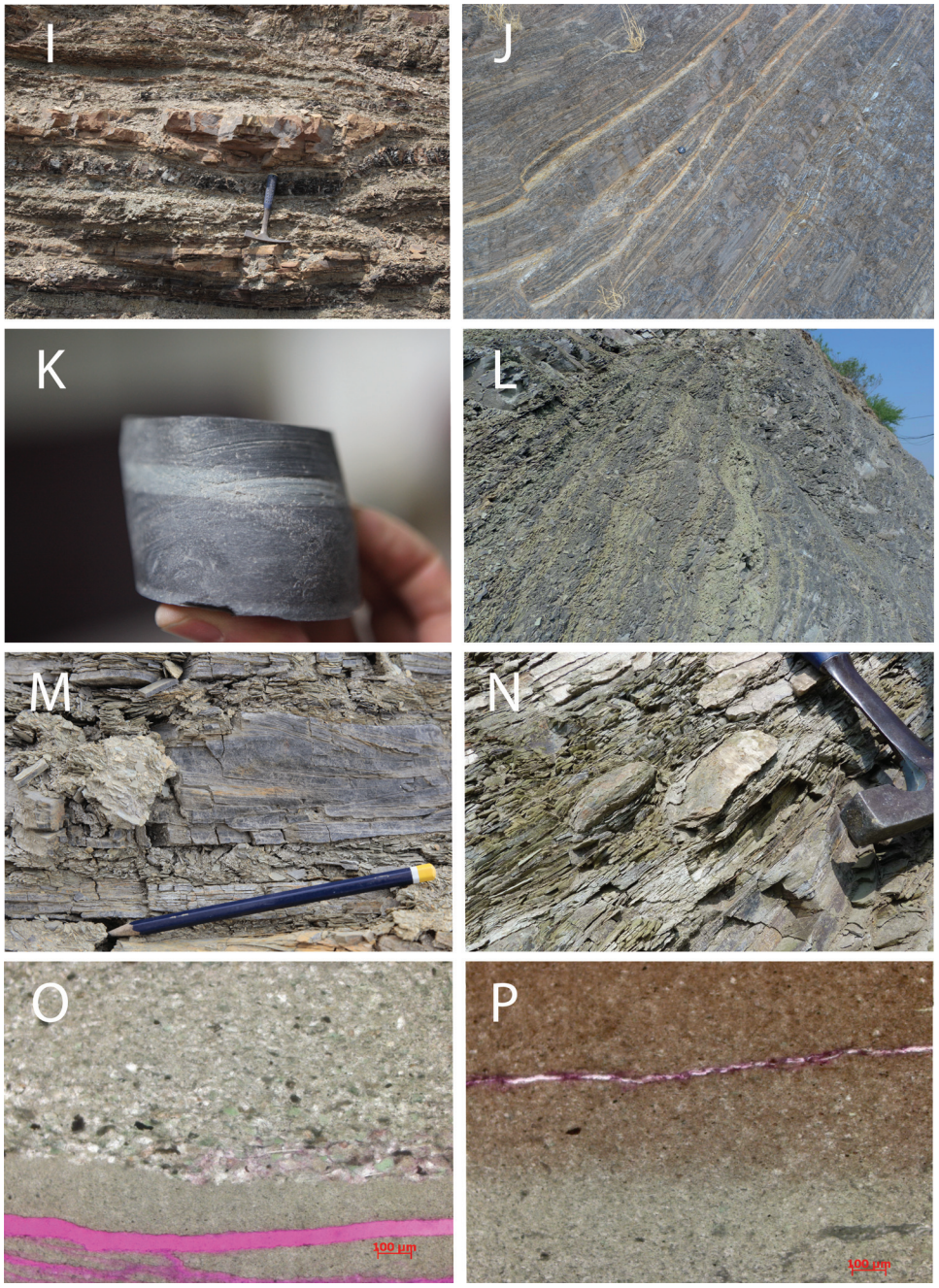

Fig. 3. (continued) (I) Carbonate layers and concretions sandwiched between layered black shales at the bottom of unit 2, (J) typical unit 2 black shales, with four bentonite layers, (K) the beginning of green/gray shale alternation with black shales, signaling the start of unit 1, (L) transition to frequent alternations between green/gray and black shales at 40 to 45 m in unit 1, (M) cross-laminated shale at about 15 m in unit 1, (N) carbonate concretions at the top of unit 1, (O) erosional contact between turbid I and underlying muds in unit 4. Note the fining upwards in the turbidite, (P) "bleeding" of green color into overlying red sediment in unit 4.

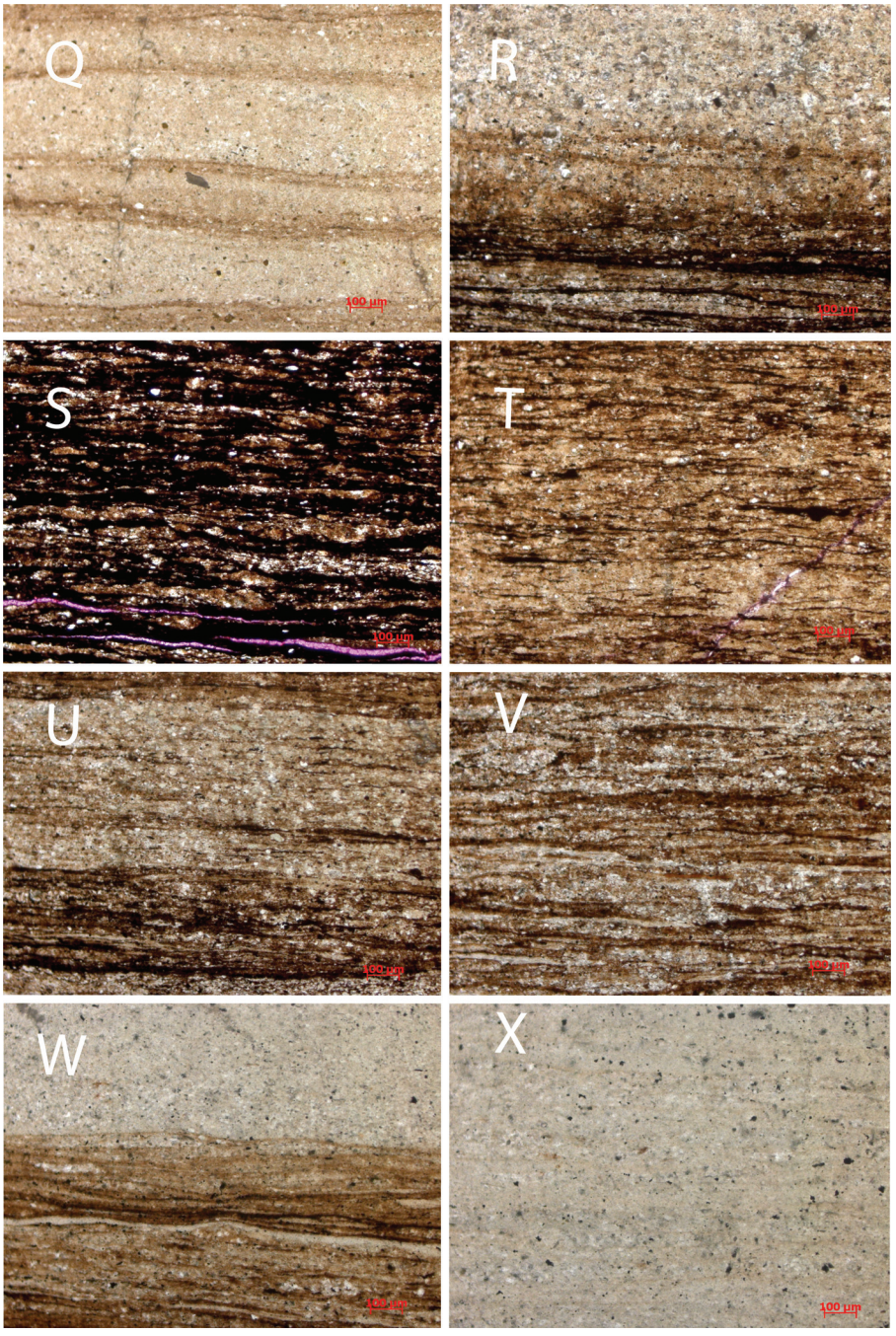

Fig. 3. (continued) (Q) Occasional organic carbon laminations within a chert unit in unit 3, (R) transition between black shale and chert in unit 3. Note that this transition does not reflect a change in background sedimentation, only a sensation of organic carbon deposition, (S) typical laminated black shale in unit 3, (T) typical laminated black shale in unit 2, (U) laminated black shale in unit 2, with an intervening relatively organic-poor layer, (V) typical organic carbon layer in unit 1, (W) transition between organic carbon rich black shales and organic carbon-poor green/gray shale in unit 1. Note that the transition does not reflect a change in lithology, (X) organic-poor green/gray shale unit in unit 1.

sandy silts to represent distal turbidites and the red layers to represent background muds, some of which may have been suspended and re-deposited during emplacement of the turbidites. We consider the red-green coloration and its meaning in more detail below.

Moving up section, the red layers disappear, and green muds alternate with green sandy silts (fig. 3F). The mud layers become thicker, and thin layers of black shale begin to appear about 10 m above the last of the red layers (fig. 3G). We take the appearance of black shale as the end of unit 4 deposition. While unit 4 contains abundant evidence for turbidites, we find no evidence for wave interaction with the sediment. The sedimentological evidence suggests unit 4 deposited at, or perhaps even well below, storm wave base.

Unit 3 begins with the appearance of black shale layers (fig. 3G). The black shale intervals are thin at first (fig. 3G), but over the span of a few meters, the black shales become more frequent, the green muds disappear, and the black shales begin to alternate with organic-poor silica-cemented sediments (fig. 3H). We will refer to these silica-cemented sediments as cherts, recognizing that they still have a substantial clastic component (Zhang and others, 2015). Most of unit 3 is characterized by alternating black shale and chert (fig. 3H) without any evidence for turbidite deposition or mass flows. Unit 3 black shales are finely laminated, with laminations interrupted by occasional thin chert intervals (figs. 3H and 3S). The alternation between black shale intervals and massive cherts can be abrupt. Thus, in thin section, black shale deposition can cease suddenly in what appears to be a background of continuously depositing sediment (fig. 3R). Still, there is also found occasional thin organic carbon-rich layers within the chert (fig. 3Q). Unit 3 is void of evidence of wave or current impingement, and is believed to represent deposition in deep quiet waters.

There is a return to green muddy silts at the top of unit 3, somewhat reminiscent of the top of unit 4. These green sediments deposited through about 20 meters of stratigraphy with frequent carbonate layers, carbonate lenses and concretions, and with occasional carbonate-cemented sandstone layers. Moving upsection, black shales begin to appear, interbedded with the carbonate layers (fig. 3I), and the black shales become continuous as the carbonates and occasional sand layers cease, signaling the transition into unit 2.

In outcrop (fig. 3J), unit 2 displays pronounced layering, most of which results from the weathering of sulfide-rich layers. Some banding, not readily observable in fresh core, also results from the differential weathering of organic-rich black shale vs less organic-rich gray shales, which themselves are not a major sediment type in the unit. Fine-scale layering is observed in thin section (figs. 3T and 3U). Unit 2 is devoid of sedimentological features indicating sediment disturbance after deposition and is thus interpreted to represent deep-water quiet depositional conditions. Overall, units 3 and 2 likely represent the deepest waters of the Xiamaling Formation.

At about 70 m depth in our stratigraphy, organic-poor green-gray shale units (fig. 3X) begin to alternate with the black shales (figs. 3V and 3K). The green-gray shale units are relatively infrequent until about 40 m depth, where they become prominent (fig. 3L). In thin section, the transition between black and green-gray shale occurs abruptly in the background of continuous sedimentation (fig. 3W). At around 15 m depth, we observe cross-laminated dark siltstones and very fine sandstones (fig. 3M), indicating the possible influence of storm waves on the sediments and a shallowing of the basin. Near the top of our stratigraphic section, carbonate layers and concretions become prominent (fig. 3N), and many of these have cemented cross-laminated sedimentary structures, possibly indicating deposition at storm wave depth. Although not observed in our stratigraphic sections, the uppermost unit 1 contains thin

stromatolitic marl, presumably reflecting even further shallowing of the basin (Fan, 2015).

As mentioned above, a bentonite layer is found in the upper part of unit 3, and a series of four ash layers are found spaced over about 1 m in unit 2 (figs. 2 and 3J) (Fan, 2015). The presence of these volcanoclastic layers has driven the suggestion that the Xiamaling Formation represents the transition from a passive margin to a back-arc basin setting (Meng and others, 2011; Qu and others, 2014). Overall, however, volcanoclastics are rare in the Xiamaling Formation, with only these two episodes of volcanoclastic deposition having been identified. Furthermore, from the bottom of unit 3, and through all of unit 2, an interval covering all of the known volcanoclastics in the Xiamaling Formation, sedimentation was in a quiet, deep, marine setting with no indication of turbidites or mass flows as might be expected to be common in a back-arc setting.

In contrast, the Xiamaling Formation, and other formations in the Jixian System (fig. 1A), are intruded by a series of diabase dikes and sills dated to between 1316 Ma and 1353 Ma (Li and others, 2009; Zhang and others, 2009; Liu and others, 2011; Zhang and others, 2012a). These intrusives are interpreted to result from continental rifting associated with breakup of the North China Craton from supercontinent Columbia (Nuna) (Zhang and others, 2012a), a process initiated after the deposition of the Xiamaling Formation (Zhang and others, 2012a).

Paleomagnetic results place the Xiamaling Formation in a tropical setting between 10°N and 30°N (Evans and Mitchell, 2011; Zhang and others, 2012b). Furthermore, spectral analysis of sediment geochemistry and color in unit 3, combined with calibrated sediment chronology, revealed repeating patterns consistent with Milankovitch cyclicity (Zhang and others, 2015). These patterns suggest that deposition of the Xiamaling Formation was heavily influenced by climate change. Overall, and as discussed fully in Zhang and others (2015), patterns of sediment geochemical variability in the Xiamaling Formation, from unit 3 to unit 1, are very similar to those observed in the Cretaceous Atlantic ocean (Wagner and others, 2013). Thus, the Cretaceous Atlantic provides a model by which the influence of climate on Xiamaling Formation deposition can be evaluated (Zhang and others, 2015). In this model, the location of the Xiamaling Formation relative to Hadley Cell circulation and the placement of the Intertropical Convergence Zone (ITCZ) are critical. Hadley cells are major cells of atmospheric circulation featuring air rising near the equator, travelling north and south and downwelling in the subtropics, typically near 30°N and S latitude. The ITCZ refers to the zone, not always at the equator, where Hadley Cell upwelling occurs. These details, and the link between climate change and water-column chemistry will be explored in more detail in sections below.

Finally, in the Xiahuayuan area, the Xiamaling Formation has experienced a remarkably low degree of thermal maturity, and was likely never heated above 90 °C (Zhang and others, 2015). While the strata have experienced a fair amount of folding, there is no evidence for hydrothermal mineralization or the late diagenetic remobilization of metals in our area of study.

MATERIALS AND METHODS

Sampling

Most of our samples come from core material obtained with a diamond-tipped bit lubricated with fresh water. Fresh water was used to reduce organic matter contamination from the coring fluids. Fresh water, however, is not a good lubricant, and our recovery of shale was rather poor, particularly in unit 3 where soft, thin, shale units alternated with much harder chert. The sediment layering, easily identified in outcrop, was often difficult to observe in the fresh core material. Therefore, correlations were

made to the outcrop stratigraphy based on a combination of geochemical comparisons and calculated stratigraphic heights based on core angle and core depth. The Xiamaling Formation was sampled in a total of 4 cores, with core 1 covering depths from 15 to 97.65 meters, core 3 covering depths from 180.78 to 254.54 meters, core 2 covering depths from 265.9 to 357.4 meters and core 4 covering depths from 352.05 to 396 meters. In the present contribution we only report geochemical results from cores 1–3, while core 4 was used to assemble part of the composite stratigraphy in figure 2, as noted above. Coring locations are found in figure A1.

For many geochemical parameters, we also report analyses from outcrop material obtained from fresh road cuts. Before collecting outcrop material, we dug some 5 to 10 cm into the rock to remove the outermost weathered layer. Overall, as shown below, when core and outcrop material is compared, there is an excellent agreement between trace element and major element geochemistry. However, sulfides were typically either partly or completely oxidized in the outcrop samples, and we view biomarker analyses as unreliable from outcrop material.

Analytical Methods

Major and trace elements.—Most major and trace element analyses for the outcrop and core materials were performed as outlined in Zhang and others (2015), Zhang and others (2017) and Zhang and others (2016b) using X-ray fluorescence (XRF) for major elements and inductively coupled plasma mass spectrometry (ICP-MS) for trace elements. The uncertainty in determination of both major elements (XRF) and trace metals (ICP) was generally < 2 percent. Some trace (U, V, Mo) and major (Fe) elements were also determined using handheld X-ray fluorescence (HHXRF) at the University of Copenhagen (UCPH) and at the University of Southern Denmark (SDU), in both cases with an Olympics Delta DP-6000 with Rh anode. For trace metals (UCPH), the HHXRF was calibrated against matrix-equivalent samples from the Xiamaling Formation whose trace metals contents were determined separately by ICP-MS calibrated against certified standards (see supplemental data tables, http://earth.geology.yale.edu/%7eajs/SupplementaryData/2017/Wang). The standard deviation for repeated determinations of the certified standard NRC PACS-2 was < 5 percent for V, 14 percent for U and 12 percent for Mo. For Fe, the HHXRF (SDU) was calibrated against 6 certified international standards and matrix-equivalent samples from the Xiamaling Formation. The Xiamaling Formation samples were calibrated with ICP-MS against certified standards as for the trace metals. The standard deviation of repeated determination of certified standards was 1 percent.

In a few cases, we also used wet chemical extraction for total Fe determination following Aller and others (1986). This method obtained 89 percent of the total iron from the NRC PACS-3 certified standard, with a relative standard deviation of < 1 percent (see supplemental tables, http://earth.geology.yale.edu/%7eajs/SupplementaryData/2017/Wang).

Organic carbon concentrations and isotopes.—Organic carbon concentrations and isotopic analyses were performed on both outcrop and core materials. All outcrop analyses were performed at the Key Laboratory of Petroleum Geochemistry (KLPG), China, and all core sample analyses were performed at SDU. For organic carbon analysis of outcrop material, samples were powdered, de-carbonated (1M HCl for 2 h), and subsequently dried. TOC concentrations were measured with a LECO CS-230HC carbon-sulfur analyzer. For outcrop samples, the isotopic composition of extracted kerogen ($\delta^{13}C_{org}$) was measured. Samples were analyzed with a Delta V Advantage mass spectrometer (Thermo Scientific Co. Ltd.) after the carbon was first combusted to carbon dioxide using a Flash EA 1112 HT. The procedure for isolating kerogen followed Durand and Nicaise (1980) and is fully described in Zhang and others (2017). The mass spectrometer was standardized with NBS-18 ($\delta^{13}C = -5.014‰$) and Chinese

standards GBW04405 ($\delta^{13}C = 0.57‰$) and GBW04407 ($\delta^{13}C = -22.4‰$) with a relative standard deviation of 0.2 permil based on replicate analyses of the standards (n = 5). For core material, organic carbon concentrations were measured on dried, decarbonated samples (1 N HCl for 2 hours at 50 °C) with a Thermo Scientific Flash EA 2000 coupled to a Thermo Scientific Delta V Advantage gas-source mass spectrometer. The AE 2000 burns the organic carbon to CO_2 and chromatographically separates the CO_2 gas. Concentrations were determined through the CO_2 peak area as recorded in the Delta V. Both concentrations and isotopic compositions were standardized against the NBS-18 standard ($\delta^{13}C = -5.014‰$) and LSVEC ($\delta^{13}C = -46.4‰$) with a standard deviation of 0.3 permil for $\delta^{13}C$ and <1 percent for total organic carbon concentration. Isotopic compositions are reported relative to the Pee Dee Belemnite (PDB).

Sulfide and sulfur isotopes.—The isotopic composition of sulfide was obtained from silver sulfide precipitated from the H_2S liberated during distillation of the pre-weighed samples by chromium reduction (Zhabina and Volkov, 1978; Canfield and others, 1986). Analyses of sulfur isotopic compositions were performed with the same mass spectrometer system used for carbon isotope analyses at SDU, where isotopic compositions were calibrated against standards IAEA S1, S2, S3 and an internal standard of sulfate ($BaSO_4$), altogether spanning a $\delta^{34}S$ range of ~50 permil (from −32.3 to +20.3 ‰). The standard deviation of repeated measurements of international standards was about 1 permil. The concentrations of sulfide in the sample were obtained by weighing the Ag_2S precipitated from the sulfide liberated during chromium reduction.

Iron speciation.—Iron speciation was performed as outlined in Poulton and Canfield (2005) and Zhang and others (2017), where four pools of highly reactive iron (FeHR) are determined. These pools include: FeCARB (siderite or ankerite), FeOX (ferrihydrite, lepidocrocite, goethite, hematite), FeMAG (magnetite or similar), and FeP (sulfidized iron, mainly pyrite). The concentrations of the iron species obtained from the chemical extractions were quantified by AAS, with a standard deviation for FeCARB of 20 percent, for FeOX and FeMAG of about 10 percent and for FeP of < 10 percent based on replicate analyses of the NRC PACS-3 sediment standard and other in house standards (see supplemental tables for repeated standard analyses, http://earth.geology.yale.edu/%7eajs/SupplementaryData/2017/Wang).

Biomarkers.—The biomarker analyses were performed on core materials at the KLPG. All glass vessels used for bitumen extraction were combusted at 700 °C in a muffle furnace to remove any organics and were then ultrasonically washed with purified water. Two hundred grams of powders were precisely weighed and extracted by Soxhlet extraction with chloroform for 8 h. The extracts (chloroform bitumen "A") were separated into various fractions including alkylated trimethyl benzenes with dominantly 2,3,6-methylation. These were identified from the aromatic fraction, with the fragment ion of m/z 134 as the base peak.

The maturity of Xiamaling Formation organic matter in the Xiahuayuan area is low (Rc ~ 0.6%, Tmax < 450 °C) (Zhang and others, 2016b), and through most of the stratigraphy, the TOC concentrations are high (>1 wt%; see below). A combination of low maturity and high TOC content enhances the prospects of preserving extractable biomarker molecules. We note, however, that even with low-maturity samples carefully collected with non-organic drilling fluids, biomarker contaminants can be introduced as samples are exposed to laboratory air during processing (Illing and others, 2014). While this is of potential concern, the highest levels of contamination found by Illing and others (2014) for C18 and C19 2,3,6-trimethyl aryl isoprenoids during laboratory sample preparation were, at maximum, some 4 to 5 orders of magnitude lower (150–400 pg onto 12 g of silicone gel) than the 0.2 to 4×10^7 pg we typically extracted from 200g of sediment (see data below). Therefore, laboratory contamination likely

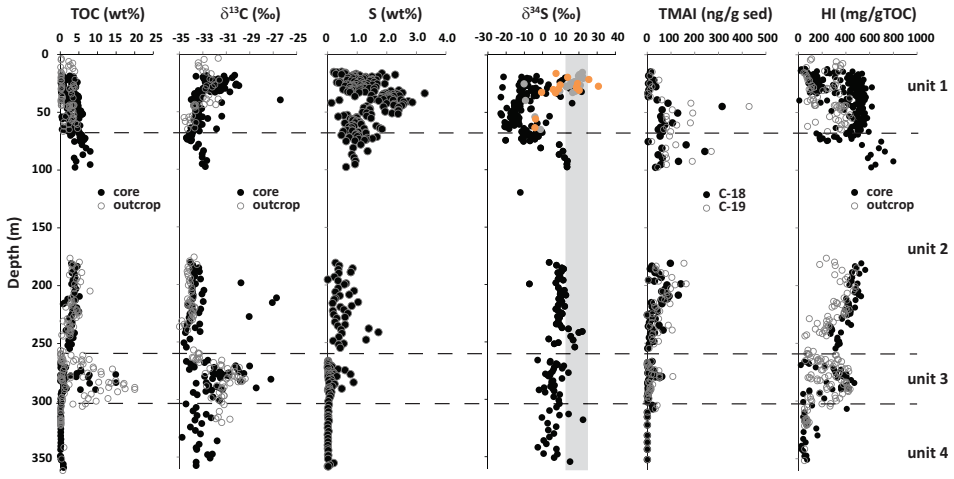

Fig. 4. Various geochemical parameters presented from the Xiamaling Formation including both outcrop and core data for many of the parameters. For the $\delta^{34}S$ results, gray dots in unit 1 represent samples with TOC contents of 0.5 to 1 wt%, and those with orange dots, TOC contents of < 0.5 wt%.

has no significant influence on our biomarker results. We also note that the biomarkers show regular stratigraphic trends which would be incompatible with either random or persistent laboratory contamination. More generally, as described by Zhang and others (2016b), the biomarker features of the Xiamaling Formation black shales and overlying Jurassic coal are very different, suggesting that biomarkers from the Xiamaling Formation do not come from younger migrated hydrocarbons.

Hydrogen Index, HI, is a measure of organic matter preservation, and is defined as S_2*100/TOC (Tissot and Welte, 1984; Espitalié, 1986). Here, S_2 represents the longer-chained, non-volatile hydrocarbons cracked and liberated during heating pyrolysis. Our samples were pyrolyzed through programmed heating in a Rock-Eval 6 instrument (Vinci Technologies, France) under a nitrogen atmosphere. Pyrolysis began at 300 °C and continued to 650 °C at a heating rate of 25 °C/min, and collected data was interpreted with software ROCKINT. The instrument was calibrated using the standard material [GBW (E) 070064~070066], and results from repeated standard analysis are presented in data tables found in the supplemental tables (http://earth.geology.yale.edu/%7eajs/SupplementaryData/2017/Wang).

RESULTS

As noted above, and as shown in figure 2, the Xiamaling Formation is informally divided into six units to encompass major changes in sediment geochemistry and/or depositional environment. We do not report geochemical data for the lowest units 5 and 6, so these will not be considered further. Also, some of the data presented here have been presented elsewhere (Zhang and others, 2015; Zhang and others, 2016b; and Zhang and others, 2017). The data sources are indicated in the supplemental tables (http://earth.geology.yale.edu/%7eajs/SupplementaryData/2017/Wang).

We begin by presenting total organic carbon (TOC) concentration data. In unit 4, the concentrations of TOC are very low, independently of whether the sediments deposited as green or red shales (fig. 4). In unit 3, TOC reaches concentrations of over

20 weight percent, falling to values of 1 weight percent or less in the adjacent chert-rich layers (see also Zhang and others, 2015). As noted above, our sample recovery for shales was poor during coring in this unit, so the outcrop results are more complete and thus especially illustrative. In unit 2, the TOC concentrations range from 2 to 4 weight percent in the lower part of the unit, and 3 to 8 weight percent in the upper part. There is also a gap of about 80 m in unit 2, as part of the formation is hidden in the subsurface with no surface outcrops. This part of the unit was also inaccessible to our drilling. The thickness of this gap was estimated from the stratigraphic relationships between exposed surface outcrops. In unit 1, the TOC concentrations in the black shales range from 2 to 6 weight percent, while the green/gray shales have TOC concentrations in the range of 0.1 to 1 weight percent (see also Zhang and others, 2015, and Zhang and others, 2017).

We continue now with the concentrations of reduced sulfur. The concentrations of sulfur are very low in unit 4 (fig. 4), generally less than 0.1 weight percent. In unit 3, the high-TOC sediments tend towards higher concentrations of sulfur than the low-TOC sediments. We suspect that the sulfur-rich sediments in this unit are under represented due to poor recovery of TOC-rich shale during drilling. In outcrop samples, concentrations of sulfide are unreliable due to weathering (for example, Ahm and others, 2017) and are not reported. In unit 2, the concentrations of sulfur range from about 0.2 weight percent to 1.5 weight percent, tending towards higher concentrations in the upper part of the unit. In unit 1, sulfur reaches very high concentrations of nearly 3 weight percent, decreasing from a maximum concentration at about 45 m to lower concentrations moving upsection.

The isotopic composition of organic carbon in the Xiamaling Formation is in the range of −35 permil to −27 permil, values quite typical for the Mesoproterozoic Era (Des Marais and others, 1992), but there is significant variability between the different units (fig. 4). For unit 4, $\delta^{13}C$ values range between −35 permil and −32 permil, while even greater variability is found in unit 3 with $\delta^{13}C$ values of up to −27 permil. The $\delta^{13}C$ values in unit 2 are more consistent at −34.5 permil to −32.8 permil, with a few "outliers" to heavier values, while in unit 1, there is a general trend from lighter to heavier values moving upwards in the unit.

The $\delta^{34}S$ of sulfide sulfur is mostly in the range of 0 to 20 permil for units 4, 3 and lower part of unit 2. However, starting at the top of unit 2, and continuing into unit 1, there is a pronounced shift in $\delta^{34}S$ from about 0 permil to as low as −24 permil, with a trend towards quite mixed values approaching the top of unit 1. In upper unit 1, the most ^{34}S-enriched values are generally associated with the organic-poor sediments (fig. 4). The $\delta^{34}S$ of seawater sulfate is not well constrained at this period in Earth history, but $\delta^{34}S$ values have been estimated at about 12 permil for 1440 Ma and 25 permil for 1280 Ma (fig. 4) (Kah and others, 2004).

We now present our biomarker results. Concentrations of the C_{18} and C_{19} 2,3,6-trimethyl aryl isoprenoids (2,3,6-TMAI) have been reported previously for all of unit 3 and parts of unit 4 and 2 (Zhang and others, 2016b). These values are shown together with additional results for all of units 1 to 4 (fig. 4). To summarize, TMAI's are essentially absent in unit 4 except for a small peak at 305 to 310 m. There is also a peak in concentration in the middle of unit 3. The concentrations are low at the base of unit 2 and generally increase through this unit with the highest values at the top. The concentrations are also relatively high in the bottom of unit 1, falling to very low values at about 40 m and continuing low to the top of the unit.

Iron speciation is highly variable through the different units (fig. 5), and a detailed account of how to interpret these results is presented in the Discussion section. In unit 4, the red sediments typically have a ratio of $FeHR/FeT > 0.38$, while the green sediments, including those near the top of the unit, do not (fig. 5). The

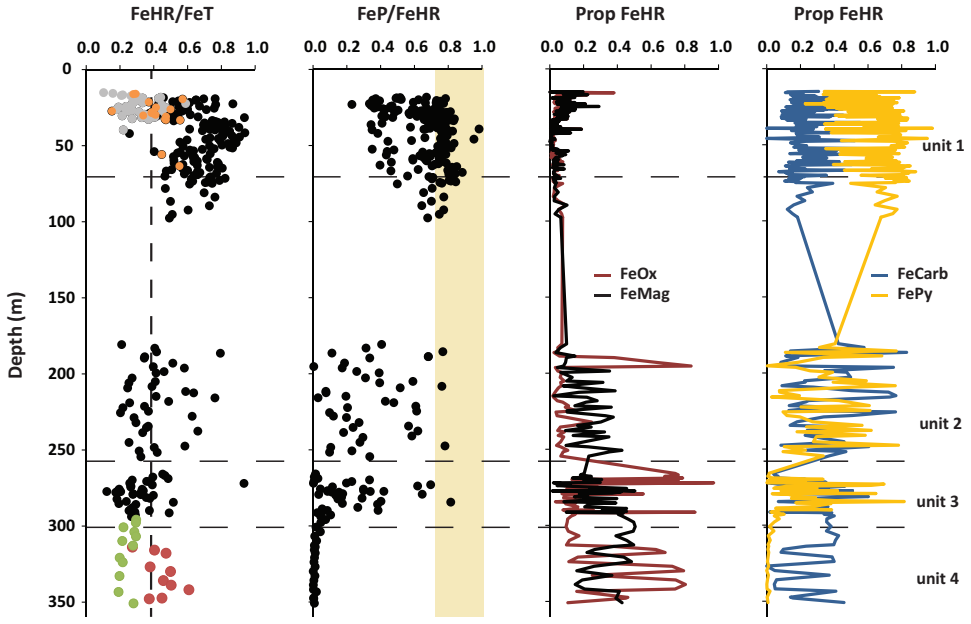

Fig. 5. Iron speciation results for the Xiamaling Formation. For FeHR/FeT in unit 1, gray dots represent samples with TOC < 0.5 wt% TOC, while orange represent samples with 0.5 to 1 wt% TOC. For unit 4, dot color reflects sediment color. See text for details.

highly reactive component of the red sediments is predominantly Fe oxides, while for the green sediments, the highly reactive component is mainly composed of Fe carbonates and magnetite (fig. 5). In unit 3, most of the sediments have a FeHR/FeT < 0.38, but occasionally, the ratio of FeHR/FeT is > 0.38. When this occurs, the FeP/FeHR ratio is generally < 0.7. The partitioning of Fe into the various highly reactive phases varies greatly in the unit (fig. 5).

Continuing to the lower part of unit 2, the ratio of FeHR/FeT is both above and below 0.38, but when above, the FeP/FeHR is generally < 0.7. In contrast, for upper unit 2, FeHR/FeT is consistently above 0.38, and FeP/FeHR is at or above 0.7. The bottom of unit 1 looks much like upper unit 2, but in the upper 40 m, and as discussed previously (Zhang and others, 2017), FeHR/FeT is generally > 0.38 in the high-TOC black shales and < 0.38 in the low TOC gray and green shales, particularly for samples with < 0.5 weight percent TOC (fig. 5). When FeHR/FeT is > 0.38 in this part of the unit, the ratio of FeP/FeT is typically > 0.7 (fig. 6).

We now consider the concentrations of the redox-sensitive metals Mo, U and V. The concentrations of these metals have been normalized to both Al and Ti to provide two different indications of enrichments over normal terrestrial background values (fig. 7). The raw metal concentrations are found in the data supplement (http://earth.geology.yale.edu/%7eajs/SupplementaryData/2017/Wang). These redox-sensitive metals show little evidence for enrichment in unit 4, but each displays strong enrichments relative to terrestrial background in unit 2, particularly in the upper part of the unit. In unit 1, the strongest enrichments are in the lower part of the unit, although less so than at the top of unit 2, and smaller, but still significant, enrichments are seen in the high-TOC black shales of the upper 40 to 45 m of the unit (fig. 8) (Zhang and others, 2017). In contrast, the low-TOC sediments (gray and green shales

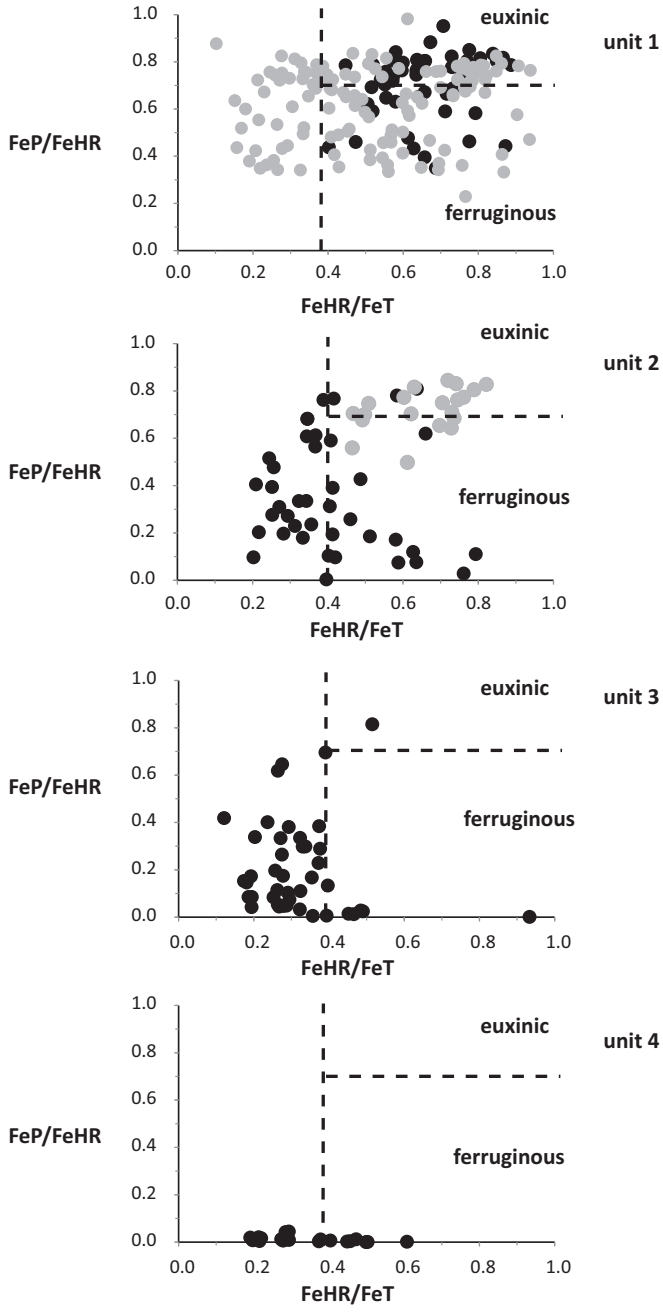

Fig. 6. Ratios of FeHR/FeT vs FeP/FeHR for the different units in the Xiamaling Formation. Also indicated are the boundaries separating euxinic from ferruginous conditions as well as the FeHR/FeT ratio of 0.38, above which anoxic depositional conditions are indicated. For unit 1, gray dots represent samples from above 45 m stratigraphic depth, while black dots represent the part of the unit below 45 m. For unit 2, gray dots represent the upper part of the unit, while black dots represent the lower part of the unit.

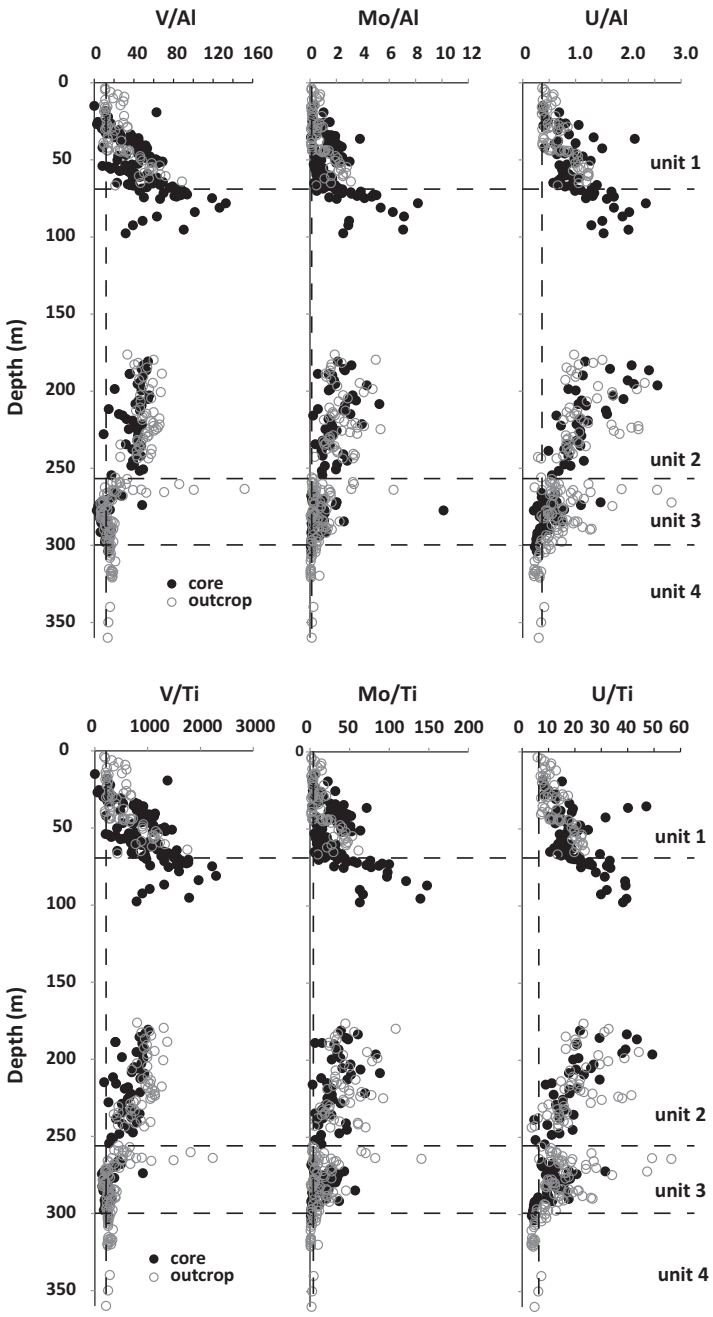

Fig. 7. Trace metal results from the Xiamaling Formation from both outcrop and core materials. Trace metal concentrations are normalized to Al in the upper panels and Ti in the lower panels. The dotted lines represent crustal average ratios from Rudnick and Gao (2003).

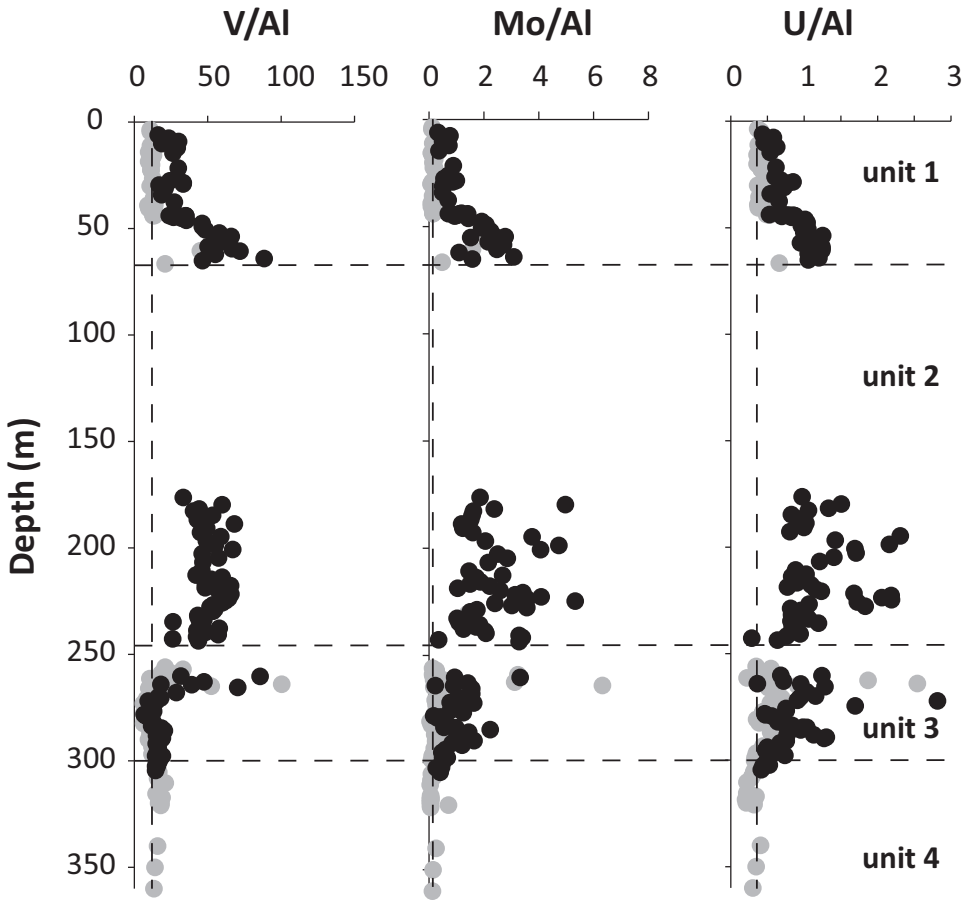

Fig. 8. Trace metal results from outcrop material where black shales (black dots) are indicated separately from low-TOC sediments types (gray dots).

of unit 1, which are concentrated mostly in the upper 40 m) show little or no enrichment in the redox-sensitive trace metals (fig. 8), as reported previously in Zhang and others (2017).

The trace metal behavior in unit 3 is quite different. In this unit, enrichments are observed in both Mo and U, particularly for the TOC-rich sediments, but through most of the unit, V is either at or below crustal-average values (figs. 7 and 8). This is true regardless of whether V is normalized to Al or to Ti (fig. 7), and regardless of whether the sample is from black shales or from cherts (fig. 8). Aspects of trace metal behavior in unit 3 have been discussed previously (Zhang and others, 2016b), and will be considered in more detail below.

DISCUSSION

Interpreting Fe Speciation

We begin with a brief introduction to the interpretation of Fe speciation results. The speciation of iron in sediment samples has frequently been used to assess the chemical nature of the waters where the sediments deposited (for example, Raiswell

and Canfield, 1998; Shen and others, 2002; Poulton and others, 2004; Poulton and Canfield, 2005; Canfield and others, 2008; Planavsky and others, 2011; Sperling and others, 2013; Sperling and others, 2014). Iron speciation is useful because anoxic depositional environments can display characteristic enrichments in so-called highly reactive iron (including iron oxides, carbonates and sulfides) to over 38 percent of the total iron in the sample. Therefore, anoxic depositional environments can have ratios of highly reactive to total iron greater than 0.38 ($FeHR/FeT > 0.38$) (Raiswell and Canfield, 1998; Raiswell and Canfield, 2012). When about 70 percent or more of the highly reactive iron is bound as sulfide (typically pyrite) ($FeP/FeHR > 0.7$), this is indicative of euxinic (sulfidic) depositional conditions (Raiswell and Canfield, 2012). When less of the highly reactive iron is bound as pyrite ($FeP/FeHR < 0.7$), this is indicative of ferruginous (iron-rich) water-column conditions.

Some anoxic environments, however, do not display the characteristic iron enrichments. For example, nitrogenous bottom waters, as found in modern anoxic oxygen-minimum zones, do not contain iron enrichments (Raiswell and Canfield, 1998). The oxic environments just adjacent to anoxic nitrogenous OMZs, however, can be enriched in highly reactive iron (Scholz and others, 2014), although these enrichments have not yet been assessed using standard iron-extraction techniques. Finally, anoxic (both sulfidic and ferruginous) depositional environments can also have ratios of $FeHR/FeT < 0.38$ (Raiswell and Canfield, 1998; Raiswell and Canfield, 2012). This means that a $FeHR/FeT < 0.38$ cannot, by itself, be used to define oxygenated water-column conditions. Such an iron speciation result, however, can be used with other geochemical information to support the interpretation of an oxygenated depositional setting. Generally, Fe speciation is best combined with other geochemical indicators to assess ancient water chemistry.

Water-Column Chemistry of Individual Units

In the following, we use our results to evaluate the evolution of water-column chemistry in the Xiamaling Formation. We will discuss each unit in turn, starting with unit 4.

Unit 4.—The same green-red colorations that we observed in the field are also observed in the core for unit 4, so our field observations of color change are not a product of weathering. As mentioned above, the red sediments generally have $FeHR/FeT > 0.38$, indicating deposition under anoxic conditions. Since the FeP/FeHR ratio is distinctly low (fig. 5), a ferruginous water column is indicated (fig. 6). As discussed above, the green-colored sediments are typically sandy silts that we interpret to represent turbidite events. As also noted, we commonly observe the green coloration to bleed into the red muddy layers, both above and below the green sandy silts (figs. 3D and 3P). In the modern ocean, turbidites typically have more reactive organic carbon than the sediments onto which they deposit (for example, Wilson and others, 1985), and we interpret the bleed down to represent the reduction of ferric iron to ferrous iron in the (once red) muds from the higher reductive capacity of the adjacent turbidites. Our chemical extractions indicate the reactive Fe in the red sediments is dominated by Fe oxides while the green sediments are dominated Fe^{2+} phases, mainly Fe carbonates (fig. 5). Similarly, the bleeding-up we observe could have resulted if the turbidites re-suspended some of the background red muds during transport, with subsequent reduction of ferric iron in the re-deposited red muds immediately above the more reducing turbidites.

Overall, our depositional model is one of pelagic sedimentation of iron-enriched, and oxidized, organic-poor muds, interspersed with the rapid deposition of more reactive sandy silt turbidites with relatively less total iron. While the iron enrichments of the red layers would seem to indicate anoxic water-column conditions, such

conditions would seem to contradict the generally low HI values in this unit (fig. 4) and the oxidized nature of the reactive Fe.

We will consider first the HI index for these samples. Low values of HI are associated with high degrees of organic matter decomposition, and, subsequently, poor organic matter preservation, as long as the samples are thermally immature and devoid of terrestrial land plant debris (Espitalie and others, 1977; Tissot and Welte, 1984). As mentioned above, the sediments we explored from the Xiamaling Formation have all experienced a low degree of thermal maturity, and they deposited some 1 billion years before the spread and diversification of terrestrial land plants.

As highlighted in a previous contribution focusing on unit 1 (Zhang and others, 2017), and in other literature (Pratt, 1984; Canfield, 1994; Kristensen and others, 1995; Aller, 2014), deposition under anoxic conditions leads to less organic matter mineralization, and consequently, enhanced organic matter preservation. Observations from unit 1 (Zhang and others, 2017) (see also below), and from other sedimentary environments from the Phanerozoic Eon (Pratt, 1984; Riboulleau and others, 2003), show that deposition under anoxic conditions typically leads to high values of HI, whereas deposition under oxygenated bottom-water conditions leads to lower values of HI, due to the more extensive aerobic decomposition of organic matter. The TOC contents of unit 4 are generally very low (0.05 to 0.4 wt%, average = 0.21 wt%) and fall on the same relationship with HI as the other units of the Xiamaling Formation (fig. 9); similar relationships between TOC and HI are also often observed in geological formations with sediments containing variable TOC contents (Pratt, 1984; Bouloubassi and others, 1999; Riboulleau and others, 2003; Sabatino and others, 2009).

While the low HI values speak to extensive organic matter decomposition, so might also the low TOC concentrations themselves. Indeed, through all of the modern major ocean basins, the concentrations of TOC captured in sediment traps to depths of 1 km or less (sampled during the Joint Global Ocean Flux Study, JGOFS) are all > 2 weight percent, with values typically in the range of 3 to 8 weight percent, or even higher (fig. 10; data from http://usjgofs.whoi.edu/mzweb/data/Honjo/sed_traps.html). Thus, marine sediments at depths of 1 km, or less, intercept particles with TOC concentrations of > 2 weight percent. Much of the organic matter settling from the photic zone in the modern ocean is associated with the carbonate and siliceous tests of phytoplankton. In the absence of these mineral tests, as would have been the case in the Mesoproterozoic oceans, one might expect even higher TOC concentrations in settling particulates. A lack of mineralized tests, however, might have also resulted in more slowly settling organic matter, potentially leading to more extensive organic matter mineralization as the particles settled (Logan and others, 1995; Zhang and others, 2016b). However, this is an unlikely explanation for the exceptionally low TOC contents of unit 4 sediments given the high TOC concentrations of other units of the Xiamaling Formation. Indeed, the range in TOC concentrations in Xiamaling Formation black shales (4–20 wt%, units 1–3, fig. 5) are similar to those found in other Proterozoic black shales (Scott and others, 2008), and in sediments from modern euxinic basins like the Black Sea (5 to 16 wt% TOC; Brumsack, 2006) and the Cariaco Basin (2–5 wt% TOC; Piper and Dean, 2002). Therefore, it would appear that sinking particulates from the Proterozoic Eon contained comparable TOC concentrations to those of today. Taken together, the low TOC contents, and associated low HI, of unit 4 sediments are completely consistent with substantial organic matter decomposition as expected under oxygenated marine bottom waters supporting extensive aerobic organic matter mineralization. Finally, the oxidized nature of the reactive Fe in the red muds is consistent with deposition into an oxygenated environment. Indeed, these red muds are reminiscent of modern deep-sea red clays depositing in well-oxygenated waters.

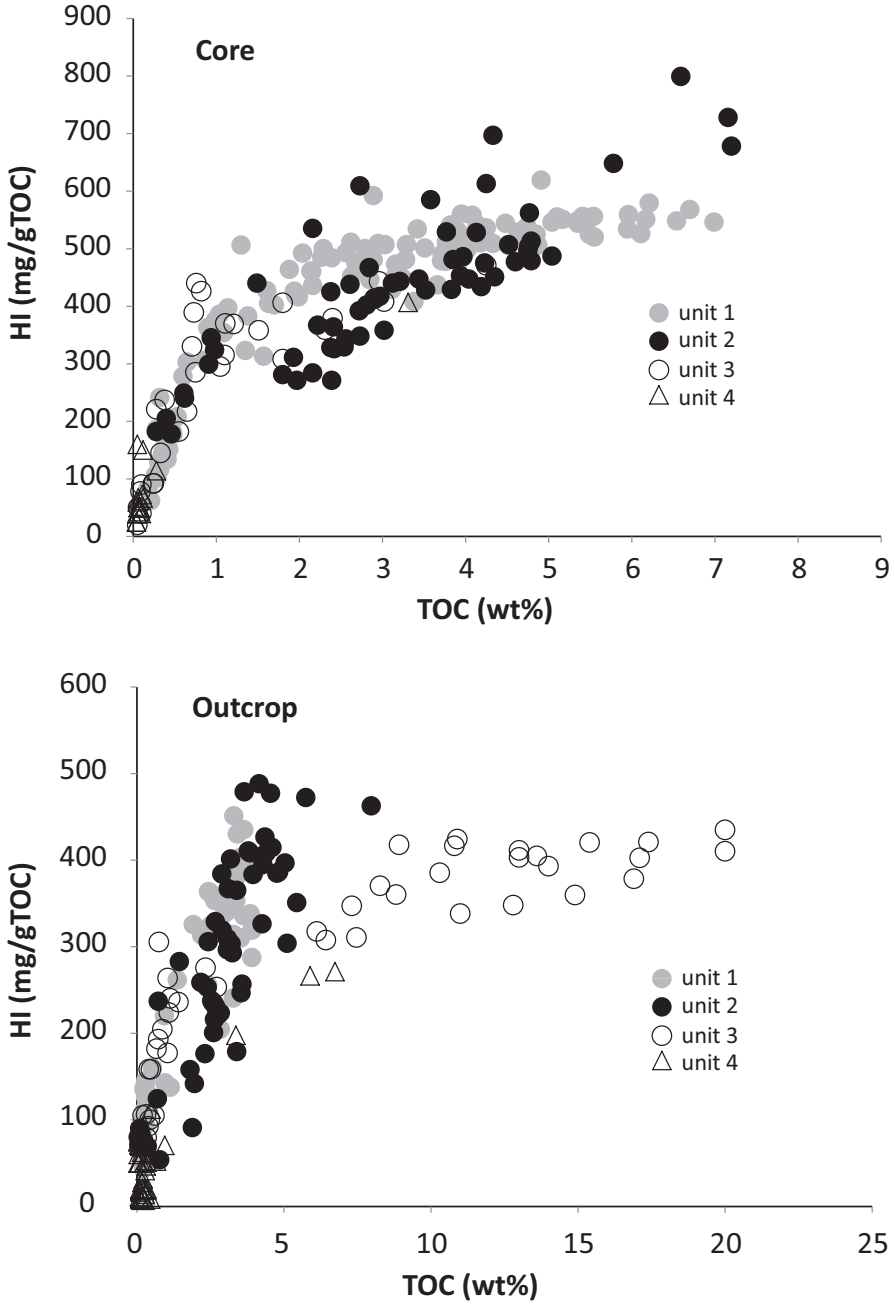

Fig. 9. HI vs. TOC for both core and outcrop samples. Outcrop samples tend to have somewhat lower HI values, which could represent the effects of weathering.

In summary, water-column conditions during the deposition of unit 4 appear to have been ferruginous, yet the waters at the sediment surface appear to have been oxygenated. The situation could have existed if a ferruginous OMZ occupied the basin,

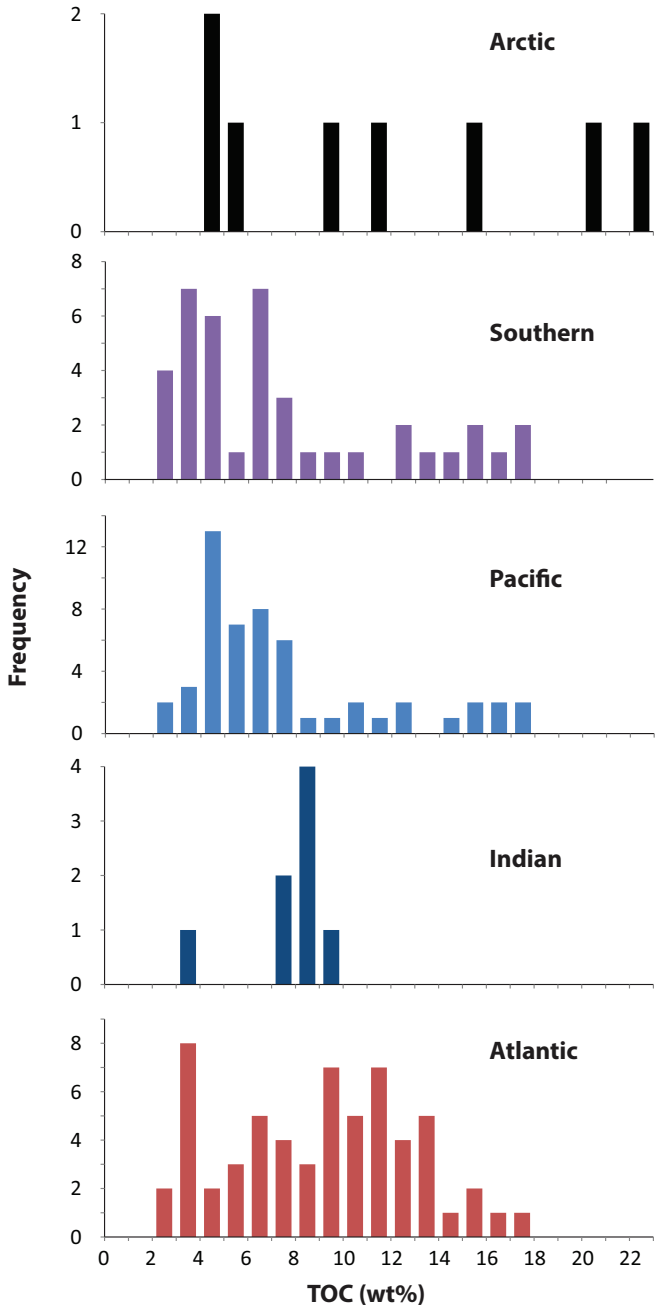

Fig. 10. Concentrations of TOC for sediment trap particles collected at depths <1000 meters during the joint Global Ocean flux study (JGOFS), separated into different ocean basins.

and if the Xiamaling Formation sediments deposited at a depth where oxygen accumulated below the overlying anoxic waters. In this way, highly reactive iron could have settled from the anoxic part of the water column and become oxidized either in

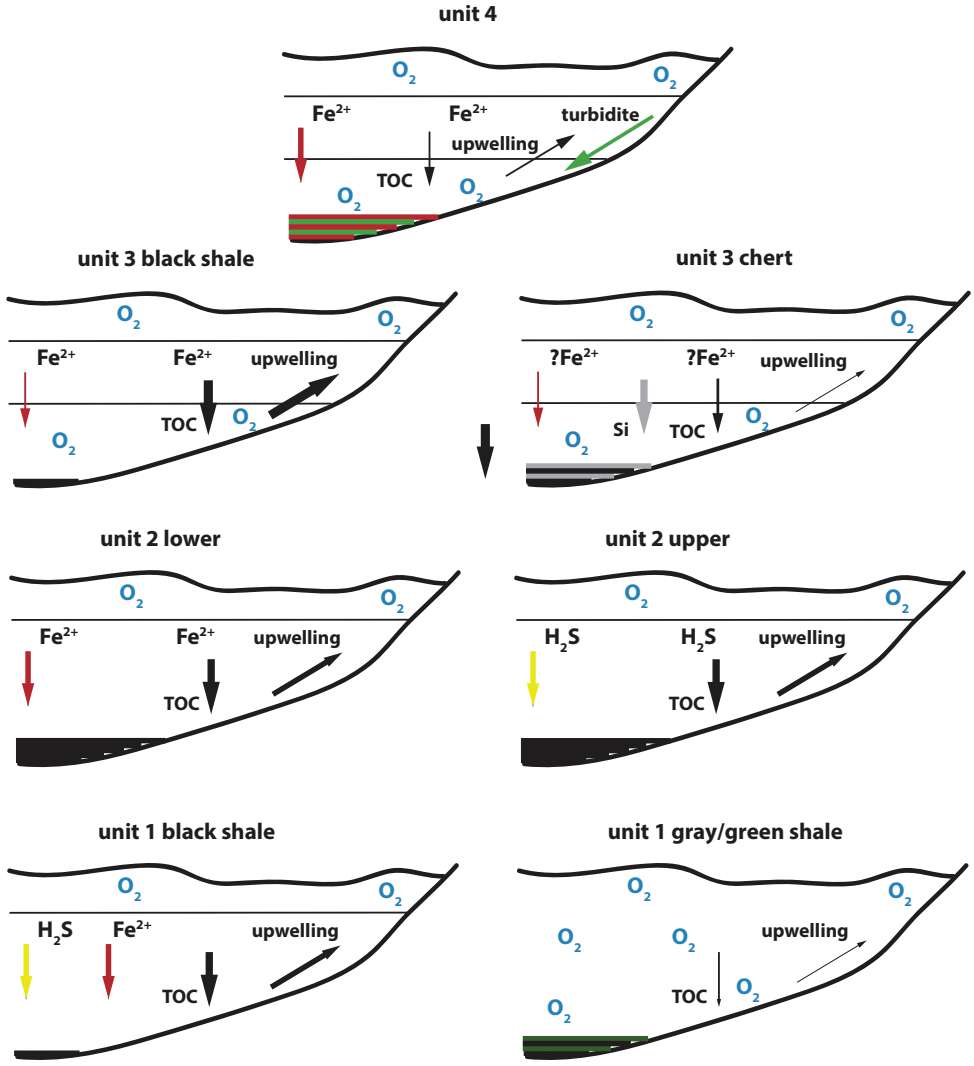

Fig. 11. Cartoon displaying depositional and chemical conditions for the different units. See text for details.

the water column or within the oxygenated surface sediments. A cartoon depicting this scenario is presented in figure 11. A somewhat analogous scenario has previously been described for unit 3 (Zhang and others, 2016b), and will be discussed in more detail below. The low concentrations of TMAI biomarkers in unit 4 sediments could reflect an absence or near-absence of anoxygenic phototrophic green-sulfur bacteria in the anoxic water column, perhaps due to phosphorus limitation in the ferruginous waters (for example, Bjerrum and Canfield, 2002). Alternatively, low TMAI content could also reflect the decomposition of these biomarkers during subsequent aerobic decomposition.

Unit 3.—As mentioned above, unit 3, likely deposited well below storm wave base and likely represents the deepest waters during deposition of the Xiamaling Formation (Fan, 2015). The geochemistry of unit 3 is quite unique and has been partly described

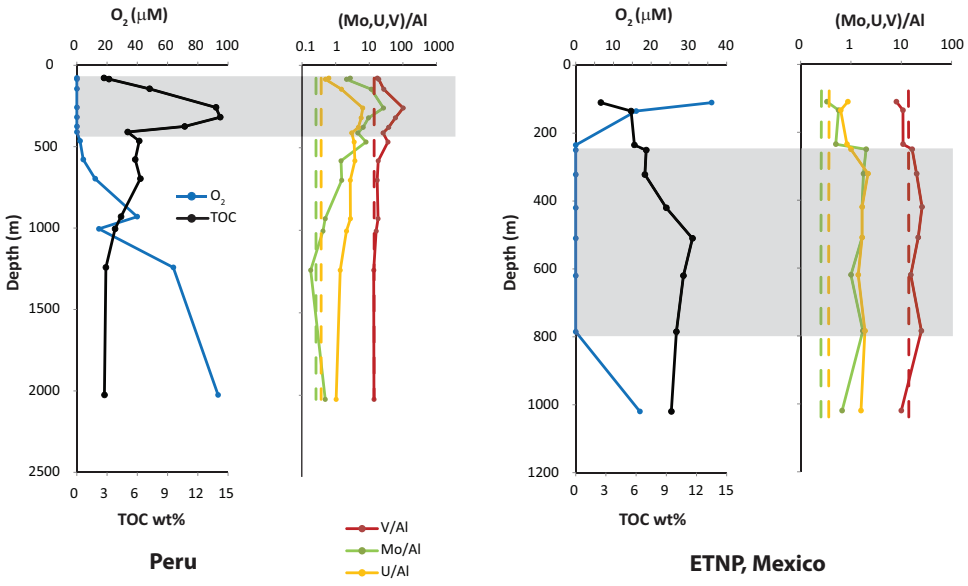

Fig. 12. Bottom water oxygen and sediment trace metal dynamics for oxygen minimum zones off the coast of Peru and Mexico. Dotted vertical lines are crustal average values color coded to the different trace metals. See text for details.

in Zhang and others (2016b). The shales of this unit are very TOC-rich and, like typical TOC-rich sediments depositing under anoxic bottom-water conditions, they are enriched in Mo and U. However, unlike any other modern examples of anoxic depositional settings, including the Black Sea (Lüschen, ms, 2004), the Cariaco Basin (Piper and Dean, 2002), the Saanich Inlet (Calvert and others, 2001), and the anoxic parts of modern OMZs (Nameroff and others, 2002; Boning and others, 2004; Scholz and others, 2011), they show no enrichment in V. Therefore, modern anoxic depositional settings do not provide an adequate model for the unit 3 geochemical environment.

It has recently been suggested that the lack of V enrichment in unit 3 sediments resulted from the input of unusually V-depleted particles (Planavsky and others, 2016). If this were true, and the sediments deposited under anoxic conditions, then the sediments somehow managed to maintain apparent crustal average (or lower) V concentrations while still enriching in V as expected during anoxic deposition. There are no modern or ancient precedents for such a scenario, and as we have argued previously (Zhang and others, 2016a), we find this very unlikely.

In contrast, there are modern analogues to the trace metal patterns observed in unit 3 of the Xiamaling Formation, and these are found in modern OMZ sediments from the eastern tropical South Pacific (ETSP), off the coast of Peru (Scholz and others, 2011), and the Eastern tropical North Pacific (ETNP) off Mazatlan, Mexico (Nameroff and others, 2002). These trace metal dynamics are best understood by comparing sediments depositing within the anoxic core of the OMZ with those depositing in oxygenated waters below the anoxic core. Thus, and as expected for anoxic water-column settings (Cochran, 1990; Calvert and Pedersen, 1993; Algeo and Lyons, 2006; Algeo and Rowe, 2012), V, Mo and U are all enriched in sediments depositing within the anoxic OMZ core in each of the sites mentioned above (fig. 12). In this anoxic OMZ core, anoxic waters directly intersect the sediments. Below the anoxic core, however, where bottom-water oxygen concentrations begin to rise, V

returns to concentrations at (ETSP), or even below (ETNP), the crustal average. In contrast, U in particular, but also Mo (especially in the ETNP), maintains enrichments above the crustal average in sediments depositing with high concentrations of TOC.

We conclude, therefore, that the patterns of trace metal enrichment seen in modern OMZs are directly analogous to those observed in unit 3 of the Xiamaling Formation. We emphasize that there are no modern examples of deposition in anoxic marine environments without V enrichment, and that all examples where V deposits in organic-rich sediments at or under crustal average values are found under oxygenated depositional conditions (Morford and Emerson, 1999; Zhang and others, 2016b).

Therefore, and as previously discussed (Zhang and others, 2016b), the geochemical evidence strongly points towards the deposition of unit 3 in oxygenated waters directly below the anoxic core of an ancient OMZ. Also, as previously discussed (Zhang and others, 2016b), an ancient OMZ interpretation is strengthened by the observation of elevated concentrations of C_{18} and C_{19} TMAIs, particularly in the middle of the unit where V depletion is the strongest. These biomarkers indicate the presence of an ancient population of anoxygenic phototrophic green-sulfur bacteria living off the oxidation of either sulfide or iron in the water column. These populations would have lived in the anoxic waters overlying the oxygenated bottom waters where unit 3 deposited (see cartoon in fig. 11).

The chert-rich sediments in unit 3 are much depleted in TOC compared to the black shales (fig. 8, compare to figs. 3Q and 3S) (Zhang and others, 2016b). These low-TOC samples tend towards low HI, indicating more extensive organic matter degradation (fig. 9). They also show the same V behavior as the black shales, while maintaining slight, but variable, enrichments in Mo and U (fig. 8; Zhang and others, 2016b). The cherts are, furthermore, enriched in TMAI biomarkers (fig. 4) (Zhang and others, 2016b). Taken together, these observations suggest that the cherts also deposited in oxygenated bottom waters, but with an overlying anoxic OMZ, similar to the periods of black shale deposition. Similarly, the reduced HI in the cherts indicates that some of the differences in TOC concentration between the black shales and cherts can be explained by more extensive organic matter degradation in the cherts. Some of the differences in TOC concentration might also relate to higher rates of primary production during black shale deposition as driven by higher winds and more intensive upwelling as discussed by Zhang and others (2015). Indeed, high rates of primary production, and the subsequent water-column decomposition of settling organic matter, could have led to more extensive oxygen depletion in the bottom waters, helping to explain the better preservation of TOC in the black shales. Thus, bottom water oxygen concentrations during chert deposition may have been higher than during black shale deposition.

Our iron speciation results are equivocal, showing limited evidence for anoxic water-column conditions through most of unit 3 (figs. 5 and 6). There are, however, occasional anoxic water-column signals, and when anoxic, indications are, except in a single instance, for ferruginous conditions. Thus, the OMZ setting of unit 3, in contrast to that of unit 4, did not deposit elevated concentrations of highly reactive iron. The reasons for this are unclear, but modern OMZ settings do not show the same iron-enrichments as observed in anoxic basins (Raiswell and Canfield, 1998). The reasons why OMZs do not show iron enrichments are also unclear, but may be related to the relatively lower concentrations of dissolved Fe^{2+} in anoxic OMZ waters compared to typical anoxic basins (Raiswell and Canfield, 2012). In modern OMZs, Fe^{2+} concentrations may be suppressed due to interactions with the nitrogen cycle (Raiswell and Canfield, 2012), where dissolved Fe^{2+} can be biologically oxidized in the reduction of nitrate (Straub and others, 1996; Straub and others, 2004). There is no evidence for a nitrogenous OMZ during the deposition of the Xiamaling Formation,

and, in contrast to modern nitrogenous OMZs, Xiamaling unit 3 supported an anoxygenic phototrophic community that likely oxidized Fe^{2+}, based on the evidence for ferruginous conditions when the water column was anoxic. Thus, despite evidence for sufficient Fe^{2+} to drive anoxygenic photosynthesis, the concentrations were too low to generate a large flux of highly reactive iron to the sediments. Or, alternatively, the Fe^{2+} might have been effectively recycled locally within the OMZ so that Fe oxyhydroxides produced during anoxygenic photosynthesis were effectively reduced and recycled within the anoxic OMZ waters. This geochemical situation might have provided a small overall flux of reactive Fe to the underlying sediments, but insufficient to produce a clear anoxic FeHR/FeT signal.

Finally, as noted above, the very top of unit 3 returns to organic-poor green and gray shale deposition. The HI index in these sediments is low, but these sediments have not been carefully explored geochemically, so we only note that the transition to unit 2 was not smooth, containing an interval with water-column conditions very different from those either typical for unit 3 or for unit 2, as explored immediately below.

Unit 2.—The shales of unit 2 have relatively high TOC concentrations of 2 to 4 weight percent (fig. 4), and they are enriched in all of the redox-sensitive trace metals, Mo, V and U, with the greatest enrichments in the uppermost part of the unit (figs. 7 and 8). This whole unit has elevated HI values (fig. 4), particularly in the core samples, which should be the most pristine. As with trace metal enrichments, the highest HI values are observed at the top of the unit. Iron speciation results show clear evidence for an anoxic depositional environment through much of the lower part, and all of the upper part of the unit (figs. 5 and 6). Since redox-sensitive trace metals and TMAI's (fig. 4, indicating the presence of water column anoxygenic phototrophs; see more below) are enriched throughout the unit, sediments with relatively low FeHR/FeT (< 0.38) likely reflect low fluxes of highly reactive iron under anoxic depositional conditions rather than a transition to an oxygenated water column. In the bottom portion of unit 2, the waters were mostly ferruginous with FeP/FeHR < 0.7 except in a few cases (figs. 5 and 6). Near the top of unit 2, in contrast, the ratio of FeP/FeHR is high, signaling the transition to a dominantly euxinic environment (figs. 5 and 6).

A pronounced transition occurs in $\delta^{34}S$ in upper unit 2, from values between 10 permil and 12 permil in the interval of 80 to 100 m, to values between -20 permil and -5 permil in the interval of 70 to 80 m (fig. 4). This transition occurs where the depositional environment was anoxic and mostly euxinic (figs. 5 and 8), and it also accompanies a rather substantial decrease in the concentrations of redox-sensitive trace metals (fig. 7). Although we have a poor understanding of the evolution of seawater sulfate $\delta^{34}S$ through the time of Xiamaling Formation deposition, it is very unlikely that the transition in $\delta^{34}S$ at the top of unit 2 reflects a dramatic change in the $\delta^{34}S$ of the sulfate reservoir. For one, the range of seawater $\delta^{34}S$ indicated on figure 4 represents the whole known range for Mesoproterozoic Era sulfate $\delta^{34}S$, and this range is much smaller than the change in pyrite $\delta^{34}S$ in the upper part of unit 2. Also, as discussed below, there are rapid changes of up to 40 permil in the $\delta^{34}S$ of pyrite in unit 1, and it is highly unlikely that these changes relate to changes in the $\delta^{34}S$ of the sulfate reservoir. Therefore, we view the range of $\delta^{34}S$ of sulfate, as indicated in figure 4, to reflect the likely $\delta^{34}S$ of seawater sulfate during Xiamaling times, and the large changes in the $\delta^{34}S$ sulfide at the top of unit 2 to reflect differences in the expression of isotope fractionation during sulfate reduction as explored immediately below.

The pyritization of reactive iron occurs quickly in the presence of sulfide (Canfield and others, 1992; Poulton and others, 2004), and, under euxinic conditions, most pyritization of reactive iron occurs in the water column (Canfield and others, 1996). Thus, small fractionations between sulfate and sulfide, as seen in the interval of unit 2 from 80 to 100 m, mean that the isotopic composition of water-column sulfide was

likely close to that of the original seawater sulfate. Furthermore, for water-column sulfide to have a $\delta^{34}S$ close to seawater sulfate requires extensive, if not nearly complete, sulfate consumption by sulfate reduction in the water column (Crowe and others, 2014; Shen and others, 2002). The high fractionations between sulfate and sulfide preserved in sediments from the interval 70 to 80 m reflect, in contrast, incomplete water-column sulfate reduction allowing sulfides formed in the water column to inherit distinctly depleted $\delta^{34}S$ values compared to the initial sulfate entering into the anoxic waters (Shen and others, 2002; Canfield and others, 2010). This change in the extent of sulfate depletion could have arisen due to either a decrease in the rate of water-column sulfate reduction, or to an increase in the concentration of sulfate entering the basin. We cannot be certain as to the cause, but the accompanying decrease in trace metal concentrations in moving to the top of unit 2 suggests less efficient trace metal removal, and this could also be associated with less sulfate reduction and less sulfide accumulation in the waters.

As mentioned above, the waters of unit 2 supported a population of anoxygenic phototrophic bacteria as evidenced by elevated concentrations of C_{18} and C_{19} TMAI biomarkers (fig. 4). These biomarkers are particularly abundant above 225 m, paralleling, to some extent, the trace metal enrichments (compare figs. 4 and 7). Overall, it seems that a population of anoxygenic phototrophs was present in the water column regardless of whether the water-column chemistry was predominantly ferruginous (lower part of unit 2) or euxinic (upper part of unit 2), and regardless of the extent of sulfate depletion in the waters. A cartoon depicting the evolution of unit 2 geochemistry is found in figure 11.

Unit 1.—As mentioned above, the boundary between unit 1 and unit 2 is not particularly clear. We have chosen to place it at 70 m where gray/green shale alternations begin. We note, however, that a further significant transition occurs at 40 to 45 m where gray/green shale-black shale alternations become much more pronounced (fig. 3L), indicating a different geochemical environment as explored below.

In many ways, the lower part of unit 1 reflects a continuation of the geochemical conditions seen in the upper part of unit 2. The bottom waters were mostly anoxic, and when anoxic, they were mostly euxinic, but also ferruginous in some instances (figs. 5 and 6). Sulfur isotopes indicate the persistence of incomplete sulfate reduction in the water column, as was also seen in the upper part of unit 2 (fig. 4), and there are no differences in the isotopic composition of sulfide between ferruginous and euxinic depositional conditions. In Lake Matano, a modern analogue environment, extensive sulfate reduction occurs in ferruginous waters just below the oxic-anoxic transition in the water column (Crowe and others, 2008; Crowe and others, 2014). By extension, it is plausible that the extent of sulfate depletion in this portion of unit 1 was similar regardless of whether the water column was sulfidic or ferruginous. If this were the case, then the factor deciding whether the waters were ferruginous or sulfidic was likely the supply rate of reactive iron to the anoxic water column, either by wind-blown dust and river-derived particulates (Canfield and others, 1996; Raiswell and Canfield, 2012), or by the dissolution and transport of ferrous iron from slope and shelf sediments intercepting the anoxic waters (Raiswell and Anderson, 2005; Lyons and Severmann, 2006; Raiswell and Canfield, 2012).

In lower unit 1 the HI is high, and redox-sensitive trace metals are similar in concentration to those seen at the very top of unit 2 (figs. 4, 7, and 8). This part of unit 1 also, like the upper part of unit 2, shows relatively large enrichments in TMAI's indicating a persistent population of anoxygenic phototrophic bacteria oxidizing either excess Fe^{2+} or H_2S in the water column. Anoxic depositional conditions dominated in lower unit 1.

We have reported previously on aspects of the geochemistry of the upper 45 m of unit 1, where a clear switching between oxic and anoxic depositional conditions is reflected in alternating TOC, HI and trace metal enrichments (figs. 4 and 8; Zhang and others, 2017) in association with the deposition of either green/gray or black shales as possibly controlled by climate (Zhang and others, 2015; Zhang and others, 2017). This switching is also reflected in alternations in FeHR/FeT, which correlate with TOC (fig. 13); TOC, in turn, correlates with $\delta^{34}S$ and trace metal concentrations (figs. 8 and 13) (Zhang and others, 2015; Zhang and others, 2017). To summarize, low TOC green/gray shales have low values of HI (fig. 9), show little if any enrichment in trace metals (figs. 8 and 13), and generally have FeHR/FeT values consistent with oxic depositional conditions (Zhang and others, 2017). In contrast, the black shales are TOC enriched, with high values of HI and trace metal enrichments. In addition, the black shales have FeHR/FeT values consistent with anoxic deposition under a mix of ferruginous and euxinic conditions (fig. 6).

We note, furthermore, that the $\delta^{34}S$ of sulfide is depleted, and generally in the range of 5 to -25 permil, when TOC is above around 1 weight percent and when FeHR/FeT gives evidence for an anoxic water column (figs. 4, 5, and 13). In contrast, the $\delta^{34}S$ of sulfide is generally enriched and mostly in the range of -5 to 25 permil when TOC is less than around 1 weight percent and where FeHR/FeT gives evidence, generally, for oxic water-column deposition (figs. 4, 5, and 13). The $\delta^{34}S$ data imply that when the water-column was anoxic, sulfate reduction was incomplete, similar to the lower part of unit 1. In contrast, when depositional conditions were oxic, sulfate reduction was far more extensive, leading to ^{34}S enrichment. More extensive sulfate depletion might be expected if sulfate reduction was restricted to sediments with a sulfate supply from overlying waters that were relatively low in sulfate concentration, as expected for this time in Earth history (Kah and others, 2004). Indeed, available estimates suggest sulfate levels of less than about 2 mM (Shen and others, 2002; Kah and others, 2004), or $<$ 7 percent of the present oceanic concentrations of 28 mM.

At around 15 m in the stratigraphy (fig. 3M), coarser, cross-laminated silt- and sandstones appear within the mudstones, some, possibly, showing signs of wave influence. Thus, unit 1, especially the upper part, may represent a regressional sequence moving up section.

Transitions in Water-Column Chemistry

Overall, the Xiamaling Formation displays many types of sedimentological and water-column chemical conditions over the course of its deposition. Unit 4 reflects oxygenated depositional conditions under a ferruginous OMZ, with periodic turbidite deposition, giving the distinct red/green color banding of the unit. Unit 3 represents continued oxic deposition, but under an OMZ with higher (but variable) rates of primary production that appear to be climate controlled (Zhang and others, 2015). This unit is not associated with turbidites, and overall, deposition was in deep waters below storm wave base. The transition from unit 3 to 2 seems to reflect a return to depositional conditions similar to those of the top of unit 4, but we did not carefully explore this transition. Unit 2 was deposited under anoxic conditions that were predominantly ferruginous in the lower part and predominantly euxinic in the upper part. An apparent reduction in the extent of water-column sulfide accumulation occurs when approaching the top of the unit. Unit 2 also deposited in deep waters with no indication of wave influence on deposition. In unit 1, mixed euxinic and ferruginous depositional conditions dominated the lower part of the unit, and at about 40 m, evidence of anoxic conditions alternate with evidence of oxygenated bottom waters. At about 15 m, there appears to be occasional wave influence on deposition that becomes evident, indicating shallowing to storm wave depth. Anoxygenic phototrophic bacteria

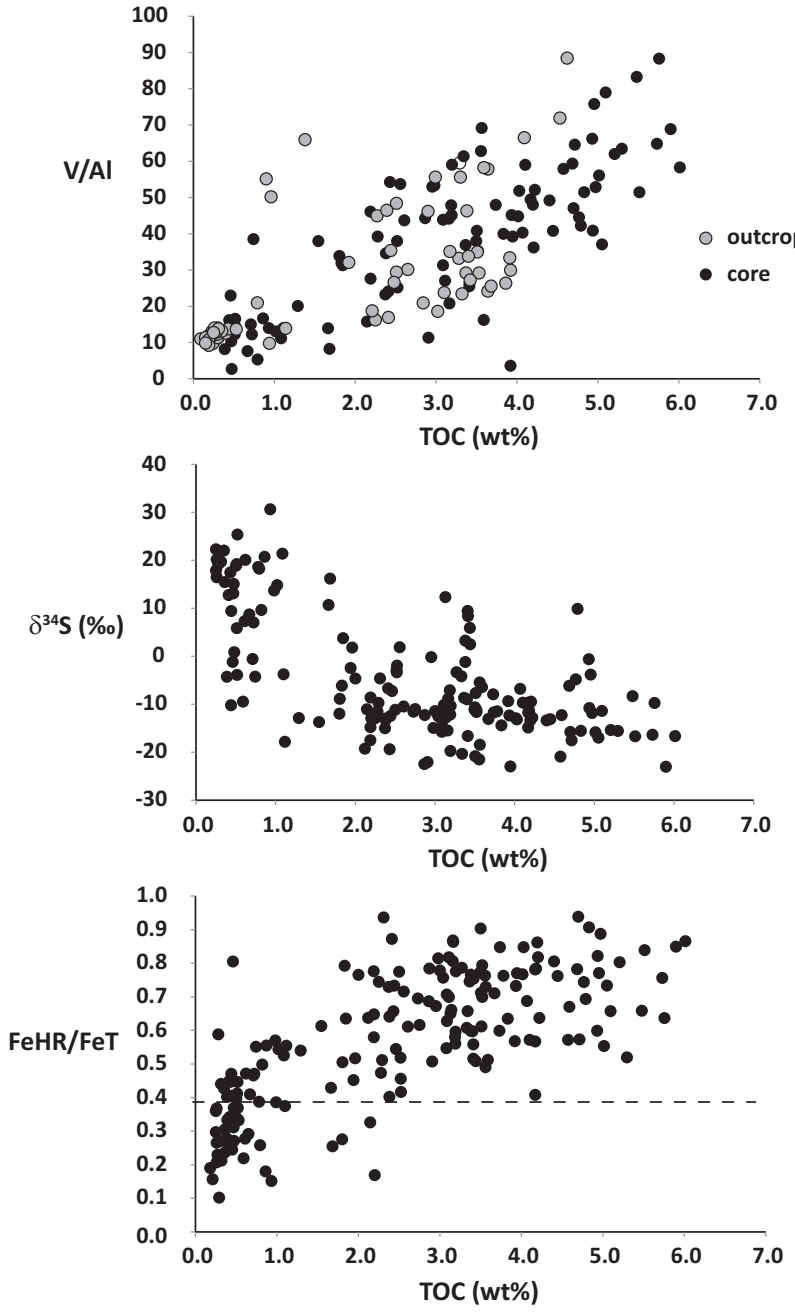

Fig. 13. V/Al, $\delta^{34}S$ and FeHR/FeT as a function of TOC in unit 1. For V/Al, both outcrop and core results are shown. The FeHR/FeT ratio of 0.38 is also indicated.

occupied the anoxic portion of the water column during deposition of all units, except unit 4, with the greatest populations during the deposition of unit 2, and lower unit 1.

As noted above, we previously developed a climate model to explain the major features of geochemical transitions between units 3 to 1 (Zhang and others, 2015). We

will expand this model to include unit 4, and we will also provide an account of the evolution of water chemistry in the context of this model.

Our model is premised on paleo-reconstructions of ancient supercontinent Columbia (Nuna) that places the Xiamaling Formation between 10°N and 30°N latitude and within the range of Hadley Cell circulation (Evans and Mitchell, 2011; Zhang and others, 2012), as this controlled patterns of wind, rainfall, and ocean circulation. Our model also draws heavily from observations of water-column chemical and sedimentological dynamics as revealed in sediments from the Cretaceous Atlantic Ocean (Kuypers and others, 2004; Hofmann and Wagner, 2011; Wagner and others, 2013). The reader is referred to Zhang and others (2015) for a full accounting of the model. But, to summarize, the fluctuating geochemical conditions of units 3 and 1 are explained by sediment deposition near the downwelling limb of an ancient Hadley Cell (Zhang and others, 2015). Here, climate would be very sensitive to the location of the ITCZ, and movement in the location of the ITCZ would alter trade wind patterns, rain intensity and ocean circulation, generating different geochemical dynamics. Thus, in our model, with a northward location of the ITCZ, the Xiamaling Formation deposited in the band of easterly trade winds that induced coastal upwelling. This situation generated high rates of primary production, an intensified OMZ, and high TOC deposition in the black shales of unit 3, while also generating anoxic conditions during black shale deposition in unit 1.

In contrast, with a more southerly location of the ITCZ, the Hadley Cell also moved southward, and the Xiamaling Formation became located under the downwelling portion of the Hadley Cell. Here trade wind intensity was reduced, limiting upwelling, and reducing the organic carbon flux to the relatively organic-poor sediments of both units 3 and 1. In the case of unit 3, geochemical evidence suggests that OMZ conditions persisted, but the reduced organic carbon flux may have allowed for higher bottom water oxygen concentrations and, hence, more extensive sedimentary organic carbon oxidation. In unit 1, with the southerly placement of the ITCZ, the water column transitioned to oxic conditions, with no evidence of an OMZ. In our model, the more southerly location of the ITCZ generated less rain in the region of Xiamaling Formation deposition, and encouraged net evaporation of surface waters and silica deposition in unit 3 (Zhang and others, 2015). There is no evidence for massive chert deposition in unit 1, but as noted earlier (Zhang and others, 2015), Si contents are slightly elevated in the gray/green shales of this unit compared to the black shales.

Unit 2 represents more stable depositional conditions, and we previously interpreted this unit to have deposited within the belt of persistent easterly trade winds, requiring a stable northerly position for the ITCZ (Zhang and others, 2015). As unit 2 reflects waters that were anoxic at the sediment surface, the transition from unit 3 to unit 2 was accompanied by either a sea-level fall, raising unit 2 into the anoxic portion of an ancient OMZ, or by a change in ocean circulation causing an overall deeping of the anoxic zone.

In moving from the lower to the upper part of unit 2, more sulfide became available relative to Fe, causing a transition from dominantly ferruginous to dominantly sulfidic conditions (figs. 5 and 6). Also, the sediments became more enriched in highly reactive-iron, implying a greater supply of reactive iron relative to the background sedimentation (figs. 5 and 6). They also become more enriched in TOC (fig. 4) and in redox-sensitive trace metals, particularly V and Mo (figs. 7 and 8). The $\delta^{34}S$ of the deposited sulfide remained ^{34}S-enriched, implying extensive sulfate depletion in the water column throughout this transition. These observations are rather anomalous, particularly the transition to euxinic conditions in moving up-section (implying iron limitation) despite a greater availability of highly reactive iron (as evidence by

higher FeHR/FeT). These observations, however, can be accommodated, at least generally, if there was an enhancement in water-column circulation (perhaps greater upwelling), relative to detrital sediment deposition, in the transition from the lower to the upper part of unit 2. Enhanced circulation could supply more reactive-iron, if the iron was sourced from the water column, as well as more nutrients to fuel primary production, and more sulfate to fuel sulfate reduction. Enhanced circulation would also supply a greater flux of trace metals. Thus, enhanced circulation could explain enrichments in highly reactive iron, trace metals and TOC concentrations, but does not, in itself, explain the transition from ferruginous to euxinic conditions. We cannot be certain, but if our model is correct, the changes in circulation elevated rates of sulfate reduction to a greater extent than they elevated the supply of reactive iron, generating a sulfide surplus. Overall, changes in circulation could have resulted from movement in the ITCZ and subsequent changes in Hadley Cell dynamics, but these details are also very uncertain.

As described above, the transition to unit 1 begins with alternations between green/gray and black shales, with such alternations becoming much more pronounced above 40 m to 45 m in our stratigraphy. These alternations in sediment type reflect transitions between oxygenated and anoxic bottom water conditions. As described previously (Zhang and others, 2015), and as mentioned above, we ascribe the transition between unit 2 and unit 1 to movement of the ITCZ placing the Xiamaling Formation again, as in unit 3, near the downwelling limb of an ancient Hadley Cell (Zhang and others, 2015). As also explained above, Hadley Cell displacement north and south, as perhaps controlled by climate change, would place the Xiamaling Formation under different regimes of trade wind direction, wind intensity, and ocean circulation, generating different bottom-water chemical conditions. Although unit 1 seems to reflect a regression to shallower waters, the water depth was still sufficient for anoxia to develop below the upper mixed layer of the ocean.

We now turn to unit 4 -. Geochemical indications are that this unit deposited under continuously oxygenated conditions, and with relatively low rates of primary production, at least lower than overlying unit 3. Also, there was apparently an active source of sediment for turbidite deposition. We can speculate that this unit deposited northward of the downwelling limb of the Hadley Cell. This could have placed the Xiamaling Formation in prevailing westerly winds, unconducive to coastal upwelling, thus supporting low productivity. In this model, the prevailing rain patterns and the specific geomorphology of continental Columbia (Nuna) supplied a source of river sediment to the shelf and slope adjacent to where the Xiamaling Formation deposited, providing the sediment source for the turbidites. This situation persisted until the Hadley Cell moved north, with the downwelling limb passing over and then settling just north of the site of Xiamaling Formation deposition. This transition in Hadley Cell placement would have initiated unit 3 deposition and generated rain patterns that delivered less river sediment to the shelf and slope, thus signaling a significant reduction in turbidite deposition.

Our model suggests that the major features of Xiamaling Formation sedimentology and water-column chemistry were driven by climate and climate change, which affected water-column productivity, water-column oxygen distribution, as well as sediment source to the basin. The major driving factor was the location of the ITCZ and the relationship of the Xiamaling Formation to Hadley Cell circulation. Generally, the ITCZ migrates towards the warming hemisphere (Broccoli and others, 2006; Schneider and others, 2014). This happens both seasonally, and in response to long-term climate change as hemispheres warm and cool. For example, during the last glacial maximum, evidence points to a 7° southward movement of the ITCZ in response to preferential cooling of the Northern Hemisphere (Arbuszewski and

others, 2013). The ITCZ is also deflected by preferential warming and cooling of landmass, relative to the adjacent ocean. Thus, on a seasonal basis, the ITCZ moves relatively little in the equatorial Pacific and Atlantic oceans, but is deflected substantially northward in Africa, and especially eastern Asia, during the Northern summer, and substantially southward in South America and Africa during the Austral summer. Around Asia, the total seasonal displacement is considerable, amounting to around 30° total latitude (Schneider and others, 2014).

Overall, changes in global temperature distribution, as well as tectonic factors like land mass distribution and continental drift, can influence the location of the ITCZ relative to any place on the globe. As noted above, the precisely dated portion of the Xiamaling Formation, representing 52 meters of stratigraphy from the top of unit 3 to the bottom part of unit 2, represents 8 million years of deposition. We have no other dating of the Xiamaling Formation, but each unit likely spans several million years. Thus, over time scales that likely represent 10's of millions of years, all of the above mentioned factors could have contributed to displacement of the ITCZ, and Hadley Cell distribution relative to where the Xiamaling Formation deposited. Although we cannot be certain as to which of these factors might have driven changes in the location of the ITCZ, we believe that the chemical dynamics observed in the Xiamaling Formation were largely controlled by them.

Mesoproterozoic Era Water-Column Chemistry and Atmospheric Oxygen

The Xiamaling Formation provides a rare window into the development of Mesoproterozoic Era ocean chemistry over a likely time span of 10's of millions of years. During this time, Xiamaling Formation bottom-water chemistry was variably oxic, ferruginous and sulfidic. This range of water chemistries encompasses all of the types previously described during the Mesoproterozoic Era (Shen and others, 2003; Planavsky and others, 2011; Gilleaudeau and Kah, 2013; Geboy and others, 2013; Sperling and others, 2015), demonstrating the potential for dynamic water-column evolution in a single location. Furthermore, water-column anoxia, at least at some depths, was typical during Xiamaling Formation deposition. This observation reinforces the idea that water-column anoxia was widespread during the Proterozoic Eon (Canfield, 1998; Planavsky and others, 2011; Raiswell and Canfield, 2012; Canfield, 2014b; Gilleaudeau and Kah, 2015; Sperling and others, 2015), which is generally taken to indicate considerably lower atmospheric oxygen levels compared to today, and compared to the Phanerozoic Eon in general (Canfield, 1998; Canfield, 2014a; Canfield, 2014b; Lyons and others, 2014; Sperling and others, 2015).

Still, the Xiamaling Formation displays evidence for bottom-water oxygenation during the deposition of units 4, 3 and 1. Previous studies have utilized the geochemical features of units 3 and unit 1 to develop models constraining oxygen levels to > 4 percent PAL for unit 3 (Zhang and others, 2016b) and > 4 to 8 percent PAL for unit 1 (Zhang and others, 2017). Deep bottom-water oxygenation has also been reported for the roughly contemporaneous (*ca.* 1420 Ma) Kaltasy Formation from central Russia (Sperling and others, 2014), although oxygen estimates were not provided in the study. In any event, for periods of time that extended over tens of millions of years, atmospheric concentrations during the Mesoproterozoic Era were likely elevated in the range of > 4 percent PAL.

These atmospheric oxygen concentrations are considerably higher than the minimum oxygen constraint for Mesoproterozoic atmospheres of < 0.1 percent PAL provided by chromium isotope systematics (Planavsky and others, 2014). In particular, the lack of fractionated Cr associated with the deposition of iron stones has been argued to indicate a lack of oxidative weathering of Cr on the continents and thus low atmospheric oxygen levels (Planavsky and others, 2014). This earlier study has been

updated with the analyses of shale-hosted Cr that also display low fractionations during the Mesoproterozoic Era (Cole and others, 2016). We still, however, maintain our earlier concerns (Zhang and others, 2016a) that the authigenic Cr component of the Mesoproterozoic samples analyzed by Planavsky and others (2014), and also Cole and others (2016), is small.

To evaluate the results of Cole and others (2016), we plot the δ^{53}Cr vs the Cr/Ti ratio in their whole rock samples and add to this data from modern oxic (deep sea) and anoxic (Cariaco Basin and Peru upwelling region) environments (data from Gueguen and others, 2016) (fig. 14). The Cr/Ti range for crustal rocks is taken from Cole and others (2016) and is indicated on the plot (fig. 14). Ratios exceeding the crustal average might be taken as evidence for authigenic Cr enrichment. The Cr/Ti for Mesoproterozoic Era samples, however, all plot in the range indicated for crustal rocks, and in the same range seen for modern oxic sediments, which have been argued to house no authigenic Cr component (Gueguen and others, 2016). Modern oxic sediments and Mesoproterozoic Era shales also share a similar range in δ^{53}Cr and, thus, there is no indication from these data that the Mesoproterozoic shales analyzed by Cole and others (2016) contain an authigenic Cr component. In contrast, sediments from modern anoxic environments, and many Neoproterozoic and Phanerozoic shales (Cole and others, 2016, although there is a limited number of these) display elevated Cr/Ti, and these tend to show δ^{53}Cr enrichments (fig. 14).

Cole and others (2016) also employed a chemical leaching procedure to selectively remove possible authigenic Cr phases. The selectivity of this extraction procedure was not evaluated, but results showed a similar δ^{53}Cr for the whole rock samples and the leachate (fig. 14) for rocks of Mesoproterozoic age. These values were also similar to the crustal average. The same procedure was used to leach Cr from modern oxic sediments (Gueguen and others, 2016) (fig. 14). The δ^{53}Cr of the leachates from these sediments is also similar to the whole-rock values and to the crustal average (Gueguen and others, 2016), with no evidence of an authigenic marine component (fig. 14). We conclude, therefore, that the similar isotopic compositions observed between whole rock samples and leachates of the Mesoproterozoic aged shales in Cole and others (2016) could have originated from the non-specific leaching of detrital Cr, as was apparently the case for the modern oxic sediments. This analysis does not prove that there was no authigenic Cr in the Mesoproterozoic shales analyzed by Cole and others (2016), but it does demonstrate that their results are completely compatible with a detrital source for the Cr. If so, these Mesoproterozoic-aged, shale-hosted δ^{53}Cr values contain no information about the evolution of atmospheric and ocean chemistry. We highlight that Cole and others (2016) also analyzed samples from the Xiamaling Formation. These samples showed crustal average Cr contents and δ^{53}Cr values, implying very low atmospheric oxygen levels, but during a time window when our analyses suggest concentrations of atmospheric oxygen of $>$ 4 to 8 percent PAL (Zhang and others, 2016a; Zhang and others, 2017).

Furthermore, we note that highly fractionated δ^{53}Cr values of up to 1.7 permil were found for Cr hosted in a number of carbonates ranging in age from 900 to 1100 Ma (Gilleaudeau and others, 2016). Prior to analyses, these carbonates were carefully screened for diagenetic influence, and, after analysis, for detrital contamination (Gilleaudeau and others, 2016). These highly fractionated values would indicate active oxidative weathering of Cr in the time window from 900 to 1100 Ma, and for atmospheric oxygen levels considerably greater than those implied by the results of Planavsky and others (2014), and Cole and others (2016). Thus, there is mounting evidence for elevated concentrations of atmospheric oxygen for protracted periods of time during the Mesoproterozoic Era.

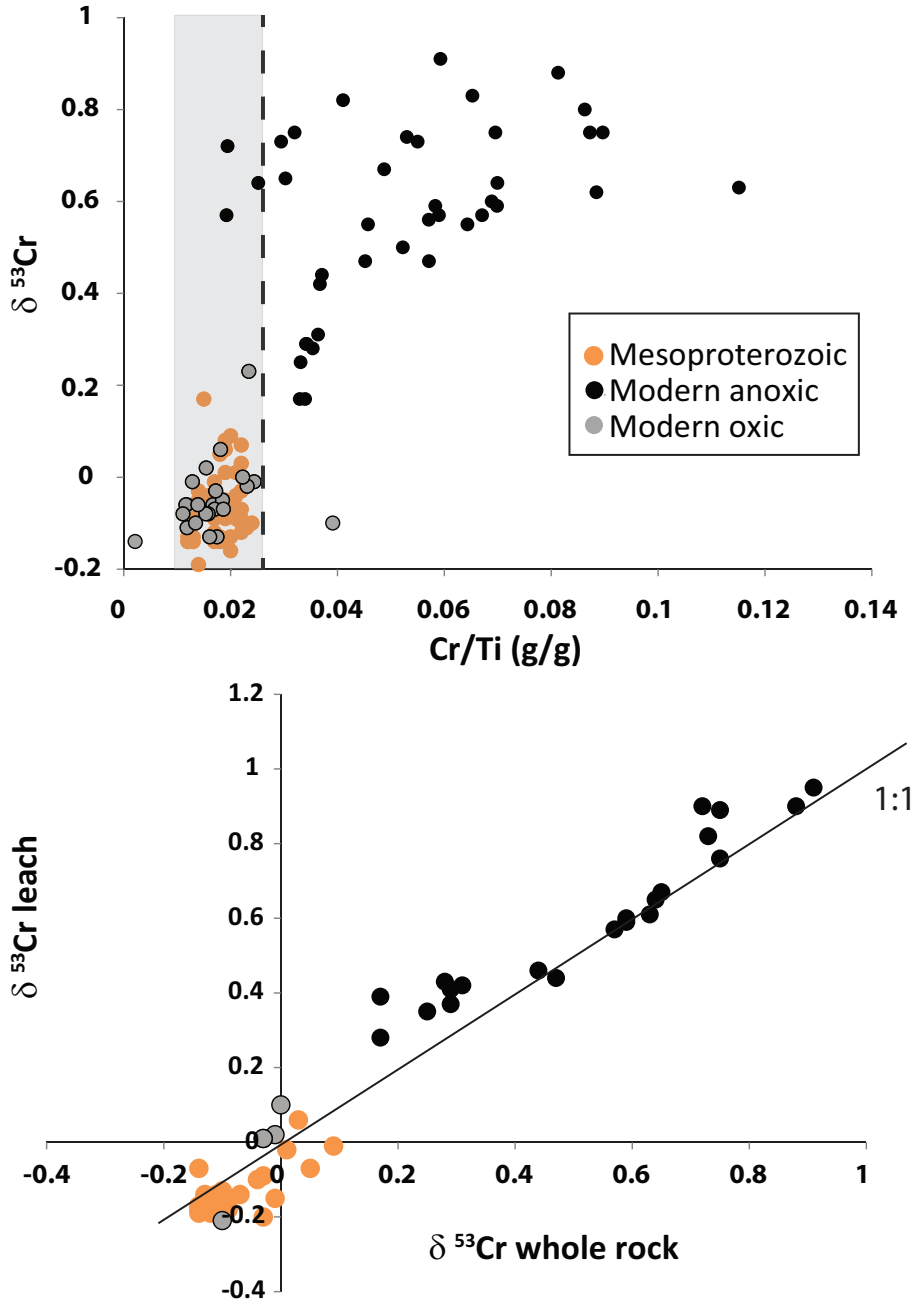

Fig. 14. Upper panel; whole rock concentrations of Cr/Ti plotted against the isotopic composition of chromium for a variety of modern sediments in oxic and anoxic environments, and from ancient shales. Lower panel; comparison of the isotopic composition of Cr from whole rock samples and solutions obtained from a chemical leaching procedure. Data from Cole and others (2016) and Gueguen and others (2016).

CONCLUSIONS

The Xiamaling Formation is a remarkable sedimentary unit deposited over what were likely 10's of millions of years on a passive continental margin. The low thermal maturity and excellent preservation of these rocks allow their organic and inorganic geochemical exploration. Overall, we evaluated four units of the Xiamaling Formation, and each unit represented distinct geochemical characteristics reflecting different water-column chemical environments. We argue that the major controls on water-column chemistry were climate, controlling rates of upwelling and the dynamics of ocean circulation, and climate change, controlling changes in water-column chemical dynamics within and between individual units. In our model, placement of the Xiamaling Formation relative to atmospheric Hadley Cell dynamics is critical in controlling the major features of water chemistry within each unit. We argue that changes in Hadley Cell placement were controlled by both long and short-term climate change, and, on long time scales, possibly also tectonic factors like continental drift.

Although water-column chemistry was dynamic, water-column anoxia was common, if not typical. This observation reinforces the consensus that ocean anoxia was much more widespread during the Mesoproterozoic Era than during the Phanerozoic Eon. Suppressed atmospheric oxygen concentrations compared to today would be one way to maintain widespread anoxic water-column conditions, and this was likely true. Still, the Xiamaling Formation displays evidence for bottom-water oxygen in three of the four units we explored. Previous modeling of oxygen dynamics in two of these units provide minimum atmospheric oxygen constraints of $>$ 4 to 8 percent PAL.

We can speculate whether the elevated oxygen levels indicated over the time span of Xiamaling Formation deposition were typical or unusual for the Mesoproterozoic Era. Hopefully, further study on other well-preserved Mesoproterozoic sections will help to answer this. However, high chromium isotope fractionations preserved in carbonates from 900 to 1100 Ma suggest that elevated global oxygen levels persisted at other times during the Mesoproterozoic Era. One may argue, of course, that the Xiamaling Formation and the late Mesoproterozoic carbonates with highly fractionated Cr only really speak to the time intervals represented by these studies. This is a valid point. However, we note that atmospheric oxygen is controlled by the kinetic balance between those processes producing oxygen and those processes consuming it. Strong negative feedbacks are associated with these processes and act to help regulate oxygen within some bounds (Canfield, 2014a). Understanding the regulation of Mesoproterozoic Era oxygen concentrations will help us to understand whether the oxygen levels indicated in the Xiamaling Formation are aberrant or typical.

ACKNOWLEDGMENTS

The authors wish to acknowledge funding from the Danish National Research Foundation (DNRF53), the ERC (Oxygen grant #267233), the Villum Foundation (Grant 16518), the Danish Council for Independent Research, as well as discussions with Daniel Mills, the very helpful reviews of Erik Sperling and an anonymous reviewer and the expert laboratory skills of Heidi Grøn Jensen and Dina Holmgaard Skov. We also acknowledge generous funding from the State Key Program of National Natural Science Foundation of China (41530317), the Scientific Research and Technological Development Project of China National Petroleum Corporation (CNPC 2016A-0204), and National Science and Technology Major Project (2016ZX05004-001).

APPENDIX

Fig. A1. Map showing location of coring and outcrop sites for the Xiamaling Formation in the Xiahuayuan area.

REFERENCES

Ahm, A.-S. C., Bjerrum, C. J., and Hammarlund, E. U., 2017, Disentangling the record of diagenesis, local redox conditions, and global seawater chemistry during the latest Ordovician glaciation: Earth and Planetary Science Letters, v. 459, p. 145–156, https://doi.org/10.1016/j.epsl.2016.09.049

Algeo, T. J., and Lyons, T. W., 2006, Mo-total organic carbon covariation in modern anoxic marine environments: Implications for analysis of paleoredox and paleohydrographic conditions: Paleoceanography, v. 21, n. 1, https://doi.org/10.1029/2004PA001112

Algeo, T. J., and Rowe, H., 2012, Paleoceanographic applications of trace-metal concentration data: Chemical Geology, v. 324, p. 6–18, https://doi.org/10.1016/j.chemgeo.2011.09.002

Aller, R. C., 2014, Sedimentary diagenesis, depositional environments, and benthic fluxes, *in* Mottl, M. J., and Elderfield, editors, The Oceans and Marine Geochemistry: Amsterdam, Elsevier, Treatise on Geochemistry, second editon, v. 8, p. 293–334, https://doi.org/10.1016/B978-0-08-095975-7.00611-2

Aller, R. C., Mackin, J. E., and Cox, R. T., Jr., 1986, Diagenesis of Fe and S in Amazon inner shelf muds: Apparent dominance of Fe reduction and implications for the genesis of ironstones: Continental Shelf Research, v. 6, n. 1–2, p. 263–289, https://doi.org/10.1016/0278-4343(86)90064-6

Anderson, T. F., and Raiswell, R., 2004, Sources and mechanisms for the enrichment of highly reactive iron in euxinic Black Sea sediments: American Journal of Science, v. 304, n. 3, p. 203–233, https://doi.org/10.2475/ajs.304.3.203

Arbuszewski, J. A., deMenocal, P. B., Cléroux, C., Bradtmiller, L., and Mix, A., 2013, Meridional shifts of the Atlantic intertropical convergence zone since the Last Glacial Maximum: Nature Geoscience, v. 6, p. 959–962, https://doi.org/10.1038/ngeo1961

Barnes, C. E., and Cochran, J. K., 1990, Uranium removal in oceanic sediments in the oceanic U balance: Earth and Planetary Science Letters, v. 97, n. 1–2, p. 94–101, https://doi.org/10.1016/0012-821X(90)90101-3

Bjerrum, C. J., and Canfield, D. E., 2002, Ocean productivity before about 1.9 Gyr ago limited by phosphorus adsorption onto iron oxides: Nature, v. 417, p. 159–162, https://doi.org/10.1038/417159a

Boning, P., Brumsack, H. J., Böttcher, M. E., Schnetger, B., Kriete, C., Kallmeyer, J., and Borchers, S. L.,

2004, Geochemistry of Peruvian near-surface sediments: Geochimica et Cosmochimica Acta, v. 68, n. 21, p. 4429–4451, https://doi.org/10.1016/j.gca.2004.04.027
Bouloubassi, I., Rullkötter, J., and Meyers, P. A., 1999, Origin and transformation of organic matter in Pliocene-Pleistocene Mediterranean sapropels: Organic geochemical evidence reviewed: Marine Geology, v. 153, n. 1–4, p. 177–197, https://doi.org/10.1016/S0025-3227(98)00082-6
Broccoli, A. J., Dahl, K. A., and Stouffer, R. J., 2006, Response of the ITCZ to Northern Hemisphere cooling: Geophysical Research Letters, v. 33, n. 1, https://doi.org/10.1029/2005GL024546
Brumsack, H. J., 2006, The trace metal content of recent organic carbon-rich sediments: Implications for Cretaceous black shale formation: Palaeogeography, Palaeoclimatology, Palaeoecology, v. 232, n. 2–4, p. 344–361, https://doi.org/10.1016/j.palaeo.2005.05.011
Butterfield, N. J., 2000, Bangiomorpha pubescens n. gen., n. sp.: Implications for the evolution of sex, multicellularity, and the Mesoprotenterozoic/Neoprtoterozoic radiation of eukaryotes: Paleobiology, v. 26, n. 3, p. 386–404, https://doi.org/10.1666/0094-8373(2000)026<0386:BPNGNS>2.0.CO;2
——— 2015, Early evolution of the Eukaryota: Palaeontology, v. 58, n. 1, p. 5–17, https://doi.org/10.1111/pala.12139
Calvert, S. E., and Pedersen, T. F., 1993, Geochemistry of recent oxic and anoxic marine-sediments: Implications for the geological record: Marine Geology, v. 113, n. 1–2, p. 67–88, https://doi.org/10.1016/0025-3227(93)90150-T
Calvert, S. E., Pedersen, T. F., and Karlin, R. E., 2001, Geochemical and isotopic evidence for post-glacial palaeoceanographic changes in Saanich Inlet, British Columbia: Marine Geology, v. 174, n. 1–4, p. 287–305, https://doi.org/10.1016/S0025-3227(00)00156-0
Canfield, D. E., 1994, Factors influencing organic carbon preservation in marine sediments: Chemical Geology, v. 114, n. 3–4, p. 315–329, https://doi.org/10.1016/0009-2541(94)90061-2
——— 1998, A new model for Proterozoic ocean chemistry: Nature, v. 396, p. 450–453, https://doi.org/10.1038/24839
——— 2014a, Oxygen: A Four Billion Year History: Princeton, New Jersey, Princeton University Press, 216 p.
——— 2014b, Proterozoic atmospheric oxygen, *in* Farquhar, J., editor, The Atmosphere-History: Amsterdam, Springer, Treatise on Geochemistry, Second Edition, v. 6, p. 197–216, https://doi.org/10.1016/B978-0-08-095975-7.01308-5
Canfield, D. E., Raiswell, R., Westrich, J. T., Reaves, C. M., and Berner, R. A., 1986, The use of chromium reduction in the analysis of reduced inorganic sulfur in sediments and shales: Chemical Geology, v. 54, n. 1–2, p. 149–155, https://doi.org/10.1016/0009-2541(86)90078-1
Canfield, D. E., Raiswell, R., and Bottrell, S., 1992, The reactivity of sedimentary iron minerals toward sulfide: American Journal of Science, v. 292, n. 9, p. 659–683, https://doi.org/10.2475/ajs.292.9.659
Canfield, D. E., Lyons, T. W., and Raiswell, R., 1996, A model for iron deposition to euxinic Black Sea sediments: American Journal of Science, v. 296, n. 7, p. 818–834, https://doi.org/10.2475/ajs.296.7.818
Canfield, D. E., Poulton, S. W., Knoll, A. H., Narbonne, G. M., Ross, G., Goldberg, T., and Strauss, H., 2008, Ferruginous conditions dominated later Neoproterozoic deep water chemistry: Science, v. 321, n. 5891, p. 949–952, https://doi.org/10.1126/science.1154499
Canfield, D. E., Farquhar, J., and Zerkle, A. L., 2010, High isotope fractionations during sulfate reduction in a low-sulfate euxinic ocean analog: Geology, v. 38, n. 5, p. 415–418, https://doi.org/10.1130/G30723.1
Cohen, P. A., and Macdonald, F. A., 2015, The Proterozoic Record of Eukaryotes: Paleobiology, v. 41, n. 4, p. 610–632, https://doi.org/10.1017/pab.2015.25
Cole, D. B., Reinhard, C. T., Wang, X., Gueguen, B., Halverson, G. P., Gibson, T., Hodgskiss, M. S. W., McKenzie, N. R., Lyons, T. W., and Planavsky, N. J., 2016, A shale-hosted Cr isotope record of low atmospheric oxygen during the Proterozoic: Geology, https://doi.org/10.1130/G37787.1
Crowe, S. A., Jones, C., Katsev, S., Magen, C., O'Neill, A. H., Sturm, A., Canfield, D. E., Haffner, G. D., Mucci, A., Sundby, B., and Fowle, D. A., 2008, Photoferrotrophs thrive in an Archean Ocean analogue: Proceedings of the National Academy of Sciences of the United States of America, v. 105, n. 41, p. 15938–15943, https://doi.org/10.1073/pnas.0805313105
Crowe, S. A., Paris, G., Katsev, S., Jones, C., Kim, S. T., Zerkle, A. L., Nomosatryo, S., Fowle, D. A., Adkins, J. F., Sessions, A. L., Farquhar, J., and Canfield, D. E., 2014, Sulfate was a trace constituent of Archean seawater: Science, v. 346, n. 6210, p. 735–739, https://doi.org/10.1126/science.1258966
Des Marais, D. J., Strauss, H., Summons, R. E., and Hayes, J. M., 1992, Carbon isotope evidence for the stepwise oxidation of the Proterozoic environment: Nature, v. 359, p. 605–609, https://doi.org/10.1038/359605a0
Duan, C., Li, Y. H., Wei, M. H., Yang, Y., Hou, K. J., Chen, X. D., and Zou, B., 2014, U-Pb dating study of detrital zircons from the Chuanlinggou Formation in the Jiangjiazhai iron deposit, North China Craton and its geological significances: Acta Petrologica Sinica, v. 30, n. 1, p. 35–48 (in Chinese with English abstract).
Durand, B., and Nicaise, G., 1980, Procedures for kerogen isolation, *in* Durand, B., editor, Kerogen-Insoluble Organic Matter from Sedimentary Rocks: Paris, Editions Technip, p. 35–54.
Espitalie, J., 1986, The use of Tmax as a maturation index for different types of organic matter: Comparison with vitrinite reflectance, *in* Burrus J., editor, Thermal Modeling in Sedimentary Basins: Paris, Editions Technip, p. 475–496.
Espitalie, J., Laporte, J. L., Madec, M., Marquis, F., Leplat, P., Paulet, J., and Boutefeu, A., 1977, Rapid method for source rocks characterization and for determination of petroleum potential and degree of evolution: Revue De L Institut Francais Du Petrole, v. 32, p. 23–42.
Evans, D. A. D., and Mitchell, R. N., 2011, Assembly and breakup of the core of Paleoproterozoic-Mesoproterozoic supercontinent Nuna: Geology, v. 39, n. 5, p. 443–446, https://doi.org/10.1130/G31654.1
Fan, W., 2015, Geological features and research progress of the Mesoproterozoic Xiamaling Formation in the North China craton: A review after nearly 100 years of study: Geological Review, v. 61, p. 1383–1406.
Gao, L. Z., Zhang, C. H., Shi, X. Y., Song, B., Wang, Z. Q., and Liu, Y. M., 2008, Mesoproterozoic age for

Xiamaling Formation in North China Plate indicated by zircon SHRIMP dating: Chinese Science Bulletin, v. 53, n. 17, p. 2665–2671, https://doi.org/10.1007/s11434-008-0340-3
Geboy, N. J., Kaufman, A. J., Walker, R. J., Misi, A., de Oliviera, T. F., Miller, K. E., Azmy, K., Kendall, B., and Poulton, S. W., 2013. Re-Os constraints and new observations of Proterozoic glacial deposits in the Vazante Group, Brazil: Precambrian Research, v. 238, p. 199–213, https://doi.org/10.1016/j.precamres.2013.10.010
Gilleaudeau, G. J., and Kah, L. C., 2013, Oceanic molybdenum drawdown by epeiric sea expansion in the Mesoproterozoic: Chemical Geology, v. 356, p. 21–37.
——— 2015, Heterogeneous redox conditions and a shallow chemocline in the Mesoproterozoic ocean: Evidence from carbon-sulfur-iron relationships: Precambrian Research, v. 257, p. 94–108, https://doi.org/10.1016/j.precamres.2014.11.030
Gilleaudeau, G. J., Frei, R., Kaufman, A. J., Kah, L. C., Azmy, K., Bartley, J. K., Chernyavskiy, P., and Knoll, A. H., 2016, Oxygenation of the mid-Proterozoic atmosphere: Clues from chromium isotopes in carbonates: Geochemical Perspectives Letters, v. 2, p. 178–187.
Gueguen, B., Reinhard, C. T., Algeo, T. J., Peterson, L. C., Nielsen, S. G., Wang, X. L., Rowe, H., and Planavsky, N. J., 2016, The chromium isotope composition of reducing and oxic marine sediments: Geochimica et Cosmochimica Acta, v. 184, p. 1–19, https://doi.org/10.1016/j.gca.2016.04.004
He, Z. J., Niu, B. G., Zhang, X. Y., Zhao, L. P., and Liu, R. Y., 2011, Discovery of the paleo-weathered mantle of the rapakivi granite covered by the Proterozoic Changzhougou Formation in the Miyun area, Beijing and their detrital zircon dating: Geological Bulletin of China, v. 30, p. 798–802.
Hofmann, A., and Wagner, T., 2011, ITCZ controls on Late Cretaceous black shale sedimentation in the tropical Atlantic Ocean: Paleoceanography, v. 26, n. 4, p. 1–11, https://doi.org/10.1029/2011PA002154
Illing, C. J., Hallmann, C., Miller, K. E., Summons, R. E., and Strauss, H., 2014, Airborne hydrocarbon contamination from laboratory atmospheres: Organic Geochemistry, v. 76, p. 26–38, https://doi.org/10.1016/j.orggeochem.2014.07.006
Javaux, E., 2011, Early eukaryotes in Precambrian oceans, *in* Gargaud, M., López-Garcia, P., and Martin, H., editors, Origins and Evolution of Life: An Astrobiological Perspective: Cambridge, England, Cambridge University Press, p. 414–449, http://hdl.handle.net/2268/37410
Kah, L. C., Lyons, T. W., and Frank, T. D., 2004, Low marine sulphate and protracted oxygenation of the Proterozoic biosphere: Nature, v. 431, p. 834–838, https://doi.org/10.1038/nature02974
Knoll, A. H., 2014, Paleobiological perspectives on early eukaryotic evolution: Cold Spring Harbor Perspectives in Biology, v. 6, n. 1, p. 1–14, https://doi.org/10.1101/cshperspect.a016121
Kristensen, E., Ahmed, S. I., and Devol, A. H., 1995, Aerobic and anaerobic decomposition of organic matter in maine sediment: Which is fastest?: Limnology and Oceanograhy, v. 40, p. 1430–1437, https://doi.org/10.4319/lo.1995.40.8.1430
Kuypers, M. M. M., Lourens, L. J., Rijpstra, W. R. C., Pancost, R. D., Nijenhuis, I. A., and Damste, J. S. S., 2004, Orbital forcing of organic carbon burial in the proto-North Atlantic during oceanic anoxic event 2: Earth and Planetary Science Letters, v. 228, n. 3–4, p. 465–482, https://doi.org/10.1016/j.epsl.2004.09.037
Li, H., Su, W. B., Zhou, H. Y., Geng, J. Z., Xiang, Z. Q., Cui, Y. R., Liu, W. C., and Lu, S. N., 2011, The base age of the Chengchengian System and in the northern North China Craton should be younger than 1670 Ma: Constraints from zircon U-Pb LA_MC_ICPMS dating of a granite porphyry dike in Miyun County, Beijing: Earth Science Frontiers, v. 18, p. 108–120 (in Chinese with English summary).
Li, H., Lu, S. N., Su, W. B., Xiang, Z. Q., Zhou, H. Y., and Zhang, Y., 2013, Recent advances in the study of the Mesoproterozoic geochronology in the North China Craton: Journal of Asian Earth Sciences, v. 72, p. 216–227, https://doi.org/10.1016/j.jseaes.2013.02.020
Li, H. K., Lu, S. N., Li, H. M., Sun, L. X., Xiang, Z. Q., Geng, J. Z., and Zhou, H. Y., 2009, Zircon and beddeleyite U-Pb dating of basic rock sills intruding Xiamaling Formation, North China: Geological Bulletin of China, v. 28, n.10, p. 1396–1404 (in Chinese with English abstract).
Li, H. K., Zhu, S. X., Xiang, Z. Q., Su, W. B., Lu, S. N., Zhou, H. Y., Geng, J. Z., Li, S., and Yang, F. J., 2010, Zircon U-Pb dating on tuff bed from Gaoyuzhuang Formation in Yanqing, Beijing: Further constraints on the new subdivision of the Mesoproterozoic stratigraphy in the northern North China Craton: Acta Petrologica Sinica, v. 26, p. 2131–2140.
Li, H. K., Su, W. B., Zhou, H. Y., Xiang, Z. Q., Tian, H., Yang, L. G., Huff, W. D., and Ettensohn, F. R., 2014, The first precise age constraints on the Jixian system of the Meso-to Neoproterozoic standard section of China: SHRIMP zircon U-Pb dating of bentonites from the Wumishan and Tieling formations in the Jixian Section, North China Craton: Acta Petrologica Sinica, v. 30, p. 2999–3012.
Liu, Y., Zhong, N., Tian, Y., Qi, W., and Mu, G., 2011, The oldest oil accumulation in China: Meso-Proterozoic Xiamaling Formation bituminous sandstone reservoirs: Petroleum Exploration Development, v. 38, p. 503–512 (in Chinese).
Logan, G. A., Hayes, J. M., Hieshima, G. B., and Summons, R. E., 1995, Terminal Proterozoic reorganization of biogeochemical cycles: Nature, v. 376, p. 53–56, https://doi.org/10.1038/376053a0
Lu, S. N., and Li, H. M., 1991, A precise U-Pb zircon age determination for the volcanics of the Dahongyu Formation, Changcheng System in Jixian: Bulletin of Chinese Academy of Geological Sciences, v. 22, p. 137–146.
Lu, S. N., Zhao, G. C., Wang, H. C., and Hao, G. J., 2008, Precambrian metamorphic basement and sedimentary cover of the North China Craton: A review: Precambrian Research, v. 160, p. 77–93.
Lüschen, H., ms, 2004, Vergleichende anorganisch-geochemische Untersuchungen an phanerozoischen Corg-reichen Sedimenten: Ein Beitrag zur Charakterisierung ihrer Fazies: Oldenburg, Germany, University of Oldenburg, Ph. D. thesis, 392 p.
Lyons, T. W., Reinhard, C. T., and Planavsky, N. J., 2014, The rise of oxygen in Earth's early ocean and atmosphere: Nature, v. 506, p. 307–315, https://doi.org/10.1038/nature13068

Lyons, T. W., and Severmann, S., 2006, A critical look at iron paleoredox proxies: New insights from modern euxinic marine basins: Geochimica et Cosmochimica Acta, v. 70, n. 23, p. 5698–5722, https://doi.org/10.1016/j.gca.2006.08.021

Meng, Q. R., Wei, H. H., Qu, Y. Q., and Ma, S. X., 2011, Stratigraphic and sedimentary records of the rift to drift evolution of the northern North China craton at the Paleo- to Mesoproterozoic transition: Gondwana Research, v. 20, n. 1, p. 205–218, https://doi.org/10.1016/j.gr.2010.12.010

Morford, J. L., and Emerson, S., 1999, The geochemistry of redox sensitive trace metals in sediments: Geochimica et Cosmochimica Acta, v. 63, n. 11–12, p. 1735–1750, https://doi.org/10.1016/S0016-7037(99)00126-X

Nameroff, T. J., Balistrieri, L. S., and Murray, J. W., 2002, Suboxic trace metal geochemistry in the eastern tropical North Pacific: Geochimica et Cosmochimica Acta, v. 66, n. 7, p. 1139–1158, https://doi.org/10.1016/S0016-7037(01)00843-2

Piper, D. Z., and Dean, W. E., 2002, Trace-element deposition in the Cariaco Basin, Venezuela shelf, under sulfate-reducing conditions: A history of the local hydrography and global climate, 20 Ka to the present: U.S. Geological Survey, Professional Paper 1670, p. 41.

Planavsky, N. J., McGoldrick, P., Scott, C. T., Li, C., Reinhard, C. T., Kelly, A. E., Chu, X., Bekker, A., Love, G. D., and Lyons, T. W., 2011, Widespread iron-rich conditions in the mid-Proterozoic ocean: Nature, v. 477, p. 448–451, https://doi.org/10.1038/nature10327

Planavsky, N. J., Reinhard, C. T., Wang, X. L., Thomson, D., McGoldrick, P., Rainbird, R. H., Johnson, T., Fischer, W. W., and Lyons, T. W., 2014, Low Mid-Proterozoic atmospheric oxygen levels and the delayed rise of animals: Science, v. 346, n. 6209, p. 635–638, https://doi.org/10.1126/science.1258410

Planavsky, N. J., Cole, D. B., Reihhard, C. T., Diamond, C., Love, G. D., Luo, G., Zhang, S., Konhauser, K. O., and Lyons, T. W., 2016, No evidence for high atmospheric oxygen levels 1,400 million years ago: Proceedings of the National Academy of Sciences of the United States of America, 113, n. 19, p. E2552–2553, https://doi.org/10.1073/pnas.1601925113

Poulton, S. W., and Canfield, D. E., 2005, Development of a sequential extraction procedure for iron: Implications for iron partitioning in continentally-derived particulates: Chemical Geology, v. 214, n. 3–4, p. 209–221, https://doi.org/10.1016/j.chemgeo.2004.09.003

Poulton, S. W., Canfield, D. E., and Fralick, P., 2004, The transition to a sulfidic ocean ~1.84 billion years ago: Nature, v. 431, p. 173–177, https://doi.org/10.1038/nature02912

Poulton, S. W., Krom, M. D., and Raiswell, R., 2004, A revised scheme for the reactivity of iron (oxyhydr)oxide minerals towards dissolved sulfide.: Geochimica et Cosmochimica Acta, v. 68, n. 18, p. 3703–3715, https://doi.org/10.1016/j.gca.2004.03.012

Pratt, L. M., 1984, Influence of Paleoenvironmental factors on preservation of organic matter in middle cretaceous Greenhorn formation, Pueblo, Colorado: The American Association of Petroleum Geologists Bulletin, v. 68, n. 9, p. 1146–1159.

Qu, Y., Pan, J., Ma, S., Lei, Z., Li, L., and Wu, G., 2014, Geological characteristics and tectonic significance of unconformities in Mesoproterozoic successions in the northern margin of the North China Block: Geoscience Frontiers, v. 5, n. 1, p. 127–138, https://doi.org/10.1016/j.gsf.2013.04.002

Raiswell, R., and Anderson, T. F., 2005, Reactive iron enrichment in sediments deposited beneath euxinic bottom waters: Constraints on supply by shelf recycling, *in* McDonald, I., Boyce, A. J., Butler, I. B., Herrington, R. J., and Polya, D. A., editors, Mineral deposits and earth evolution: Geological Society, London, Special Publications, v. 248, p. 179–194, https://doi.org/10.1144/GSL.SP.2005.248.01.10

Raiswell, R., and Canfield, D. E., 1998, Sources of iron for pyrite formation in marine sediments: American Journal of Science, v. 298, n. 3, p. 219–245, https://doi.org/10.2475/ajs.298.3.219

——— 2012, The Iron Biogeochemical Cycle Past and Present: Geochemical Perspectives, v. 1, n. 1, p. 1–220, https://doi.org/10.7185/geochempersp.1.1

Riboulleau, A., Baudin, F., Deconinck, J. F., Derenne, S., Largeau, C., and Tribovillard, N., 2003, Depositional conditions and organic matter preservation pathways in an epicontinental environment: The Upper Jurassic Kashpir Oil Shales (Volga Basin, Russia): Palaeogeography, Palaeoclimatology, Palaeoecology, v. 197, n. 3–4, p. 171–197, https://doi.org/10.1016/S0031-0182(03)00460-7

Rudnick, R. L., and Gao, S., 2003, Composition of the continental crust, *in* Rudnick, R. L., editor, The Crust: Amsterdam, Elsevier, Treatise of Geochemistry, v. 3, p. 1–64, https://doi.org/10.1016/B0-08-043751-6/03016-4

Sabatino, N., Neri, R., Bellanca, A., Jenkyns, H. C., Baudin, F., Parisi, G., and Masetti, D., 2009, Carbon-isotope records of the Early Jurassic (Toarcian) oceanic anoxic event from the Valdorbia (Umbria-Marche Apennines) and Monte Mangart (Julian Alps) sections: Palaeoceanographic and stratigraphic implications: Sedimentology, v. 56, n. 5, p. 1307–1328, https://doi.org/10.1111/j.1365-3091.2008.01035.x

Schneider, T., Bischoff, T., and Haug, G. H., 2014, Migrations and dynamics of the intertropical convergence zone: Nature, v. 513, p. 45–53, https://doi.org/10.1038/nature13636

Scholz, F., Hensen, C., Noffke, A., Rohde, A., Liebetrau, V., and Wallmann, K., 2011, Early diagenesis of redox-sensitive trace metals in the Peru upwelling area - response to ENSO-related oxygen fluctuations in the water column: Geochimica et Cosmochimica Acta, v. 75, n. 22, p. 7257–7276, https://doi.org/10.1016/j.gca.2011.08.007

Scholz, F., Severmann, S., McManus, J., and Hensen, C., 2014, Beyond the Black Sea paradigm: The sedimentary fingerprint of an open-marine iron shuttle: Geochimica et Cosmochimica Acta, v. 127, p. 368–380, https://doi.org/10.1016/j.gca.2013.11.041

Scott, C., Lyons, T. W., Bekker, A., Shen, Y., Poulton, S. W., Chu, X., and Anbar, A. D., 2008, Tracing the stepwise oxygenation of the Proterozoic ocean: Nature, v. 452, p. 456–459, https://doi.org/10.1038/nature06811

Shen, Y., Canfield, D. E., and Knoll, A. H., 2002, Middle Proterozoic ocean chemistry: Evidence from the

McArthur Basin, Northern Australia: American Journal of Science, v. 302, n. 2, p. 81–109, https://doi.org/10.2475/ajs.302.2.81
Shen, Y., Knoll, A. H., and Walter, M. R., 2003, Evidence for low sulphate and anoxia in a mid-Proterozoic marine basin: Nature, v. 423, p. 632–635, https://doi.org/10.1038/nature01651
Sperling, E. A., Halverson, G. P., Knoll, A. H., Macdonald, F. A., and Johnston, D. T., 2013, A basin redox transect at the dawn of animal life: Earth and Planetary Science Letters, v. 371–372, p. 143–155, https://doi.org/10.1016/j.epsl.2013.04.003
Sperling, E. A., Rooney, A. D., Hays, L., Sergeev, V. N., Vorob'eva, N. G., Sergeeva, N. D., Selby, D., Johnston, D. T., and Knoll, A. H., 2014, Redox heterogeneity of subsurface waters in the Mesoproterozoic ocean: Geobiology, v. 12, n. 5, p. 373–386, https://doi.org/10.1111/gbi.12091
Sperling, E. A., Wolock, C. J., Morgan, A. S., Gill, B. C., Kunzmann, M., Halverson, G. P., Macdonald, F. A., Knoll, A. H., and Johnston, D. T., 2015, Statistical analysis of iron geochemical data suggests limited late Proterozoic oxygenation: Nature, v. 523, p. 451–454, https://doi.org/10.1038/nature14589
Straub, K. L., Benz, M., Schink, B., and Widdel, F., 1996, Anaerobic, nitrate-dependent Microbial oxidation of ferrous iron: Applied and Environmnetal Microbiology, v. 62, n. 4, p. 1458–1460.
Straub, K. L., Schönhuber, W. A., Buchholz-Cleven, B. E. E., and Schink, B., 2004, Diversity of ferrous iron-oxidizing, nitrate-reducing bacteria and their involvement in oxygen-independent iron cycling: Geomicrobiology Journal, v. 21, n. 6, p. 371–378, http://dx.doi.org/10.1080/01490450490485854
Su, W. B., Li, H., Huff, W. D., Ettensohn, F. R., Zhang, S., Zhou, H. Y., and Wan, Y., 2010, SHRIMP U-Pb dating for a K-bentonite bed in the Tieling Formation, North China: Chinese Science Bulletin, v. 55, n. 29, p. 3312–3323, https://doi.org/10.1007/s11434-010-4007-5
Su, W. B., Zhang, S., Huff, W. D., Li, H., Ettensohn, F. R., Chen, X., Yang, H., Han, Y. G., Song, B., and Santosh, M., 2008, SHRIMP U-Pb ages of K-bentonite beds in the Xiamaling Formation: Implications for revised subdivision of the Meso- to Neoproterozoic history of the North China Craton: Gondwana Research, v. 14, p. 543–553.
Sun, H., Gao, L. Z., Bao, C., Chen, Y., and Liu, D., 2013, SHRIMP zircon U-Pb of Mesproterozoic Chuanlinggou Formation from Kuancheng County in Hebei Province and its geological implications: Acta Geologica Sinica, v. 87, p. 591–596 (in Chinese).
Tissot, B. P., and Welte, D. H., 1984, Petroleum formation and occurrence: New York, Springer-Verlag, 702 p., https://doi.org/10.1007/978-3-642-87813-8
Wagner, T., Hofmann, P., and Flogel, S., 2013, Marine black shale deposition and Hadley Cell dynamics: A conceptual framework for the Cretaceous Atlantic Ocean: Marine and Petroleum Geology, v. 43, p. 222–238, https://doi.org/10.1016/j.marpetgeo.2013.02.005
Wilson, T. R. S., Thomson, J., Colley, S., Hydes, D. J., Higgs, N. C., and Sørensen, J., 1985, Early organic diagenesis: The significance of progressive subsurface oxidation fronts in pelagic sediments: Geochimica et Cosmochimica Acta, v. 49, n. 3, p. 811–822, https://doi.org/10.1016/0016-7037(85)90174-7
Zhabina, N. N., and Volkov, I. I., 1978, A method of determination of various sulfur compounds in sea sediments and rocks, *in* Krumbein, W. E., editor, Environmental Biogeochemistry and Geomicrobiology: Ann Arbor, Ann Arbor Science Publishers, p. 735–746.
Zhang, S., Wang, X., Hammarlund, E. U., Wang, H., Costa, M. M., Bjerrum, C. J., Connelly, J. N., Zhang, B., Bian, L., and Canfield, D. E., 2015, Orbital forcing of climate 1.4 billion years ago: Proceedings of the National Academy of Sciences of the United States of America, v. 112, n. 12, p. E1406-E1413, https://doi.org/10.1073/pnas.1502239112
Zhang, S., Wang, X., Wang, H., Bjerrum, C. J., Hammarlund, E. U., Dahl, T. W., and Canfield, D. E., 2016a, Strong evidence for high atmospheric oxygen levels 1,400 million years ago: Proceedings of the National Academy of Sciences of the United States of America, v. 113, n. 19, p. E2552-E2553, https://doi.org/10.1073/pnas.1603982113
Zhang, S., Wang, X., Wang, H., Hammarlund, E. U., Su, J., Wang, Y., and Canfield, D. E., 2017, The oxic degradation of sedimentary organic matter 1400 Ma constrains atmospheric oxygen levels: Biogeosciences, v. 14, n. 8, p. 2133–2149, https://doi.org/10.5194/bg-14-2133-2017
Zhang, S. C., Wang, X. M., Wang, H. J., Bjerrum, C. J., Hammarlund, E. U., Costa, M. M., Connelly, J. N., Zhang, B. M., Su, J., and Canfield, D. E., 2016b, Sufficient oxygen for animal respiration 1,400 million years ago: Proceedings of the National Academy of Sciences of the United States of America, v. 113, n. 7, p. 1731–1736, https://doi.org/10.1073/pnas.1523449113
Zhang, S. H., Zhao, Y., Yang, Z. Y., He, Z. F., and Wu, H., 2009, The 1.35 Ga diabase sills from the northern North China Craton: Implications for breakup of the Columbia (Nuna) supercontinent: Earth and Planetary Science Letters, v. 288, n. 3–4, p. 588–600, https://doi.org/10.1016/j.epsl.2009.10.023
Zhang, S. H., Zhao, Y., and Santosh, M., 2012a, Mid-Mesoproterozoic bimodal magmatic rocks in the northern North China Craton: Implications for magmatism related to breakup of the Columbia supercontinent: Precambrian Research, v. 222–223, p. 339–367, https://doi.org/10.1016/j.precamres.2011.06.003
Zhang, S. H., Li, Z. X., Evans, D. A. D., Wu, H. C., Li, H. Y., and Dong, J., 2012b, Pre-Rodinia supercontinent Nuna shaping up: A global synthesis with new paleomagnetic results from North China: Earth and Planetary Science Letters, v. 353–354, p. 145–155, https://doi.org/10.1016/j.epsl.2012.07.034
Zhang, S. H., Yue, Z., Ye, H., Hu, J. M., and Wu, F., 2013, New constraints on ages of the Chuanlinggou and Tuanshanzi formations of the Chengcheng System in the Yan-Liao area in the northern North China Craton: Acta Petrologica Sinica, v. 29, n. 7, p. 2481–2490.
Zhu, S. X., Cao, R. Q., Zhao, W. J., and Liang, Y. Z., 1978, Study of stromatolites in the Sinian Suberathem of the Jixian stratotype section: Acta Geologica Sinica-English Edition, v. 52, p. 209–221.
Zhu, X., Zhang, K., Zhang, F., Gao, Z., Dong, A., Bao, C., Guo, Y., Yan, B., and HLiu, H., 2013, Discovery of siderite concretes in Mesoproterozoic Xiamaling Formation, Jiaxian Section: Geological Review, v. 59, p. 816–822.